

Leptonic Scalars and Collider Signatures in a UV-complete Model

P. S. Bhupal Dev,^a Bhaskar Dutta,^b Tathagata Ghosh,^{c,d,e} Tao Han,^e Han Qin,^e
Yongchao Zhang^f

^a*Department of Physics and McDonnell Center for the Space Sciences, Washington University, St. Louis, MO 63130, USA*

^b*Mitchell Institute for Fundamental Physics and Astronomy, Department of Physics and Astronomy, Texas A&M University, College Station, TX 77843, USA*

^c*Regional Centre for Accelerator-based Particle Physics, Harish-Chandra Research Institute, HBNI, Chhatnag Road, Jhansi, Prayagraj (Allahabad) 211019, India*

^d*Instituto de Física, Universidade de São Paulo, R. do Matao 1371, São Paulo, SP 05508-090, Brazil*

^e*PITT PACC, Department of Physics and Astronomy, University of Pittsburgh, 3941 O'Hara St., Pittsburgh, PA 15260, USA*

^f*School of Physics, Southeast University, Nanjing 211189, China*

E-mail: bdev@wustl.edu, dutta@tamu.edu, tathagataghosh@hri.res.in,
than@pitt.edu, han.qin@pitt.edu, zhangyongchao@seu.edu.cn

ABSTRACT: We study the non-standard interactions of neutrinos with light leptonic scalars (ϕ) in a global ($B - L$)-conserved ultraviolet (UV)-complete model. The model utilizes Type-II seesaw motivated neutrino interactions with an $SU(2)_L$ -triplet scalar, along with an additional singlet in the scalar sector. This UV-completion leads to an enriched spectrum and consequently new observable signatures. We examine the low-energy lepton flavor violation constraints, as well as the perturbativity and unitarity constraints on the model parameters. Then we lay out a search strategy for the unique signature of the model resulting from the leptonic scalars at the hadron colliders via the processes $H^{\pm\pm} \rightarrow W^\pm W^\pm \phi$ and $H^\pm \rightarrow W^\pm \phi$ for both small and large leptonic Yukawa coupling cases. We find that via these associated production processes at the HL-LHC, the prospects of doubly-charged scalar $H^{\pm\pm}$ can reach up to 800 (500) GeV and 1.1 (0.8) TeV at the 2σ (5σ) significance for small and large Yukawa couplings, respectively. A future 100 TeV hadron collider will further increase the mass reaches up to 3.8 (2.6) TeV and 4 (2.7) TeV, at the 2σ (5σ) significance, respectively. We also demonstrate that the mass of ϕ can be determined at about 10% accuracy at the LHC for the large Yukawa coupling case even though it escapes as missing energy from the detectors.

KEYWORDS: Neutrino self-interactions, Leptonic scalars, Large Hadron Collider, Doubly-charged scalar

Contents

1	Introduction	1
2	The model	3
2.1	Key parameters and decay channels of $H^{\pm\pm}$ and H^\pm	6
2.2	Low-energy LFV constraints	10
2.3	High-energy behavior: perturbativity and unitarity limits	10
3	Collider signatures	13
3.1	Small Yukawa coupling scenario	14
3.1.1	Cut-based analysis	15
3.1.2	BDT improvement	18
3.1.3	Mass reaches	19
3.2	Large Yukawa coupling scenario	21
3.2.1	Analysis and mass reaches	22
3.2.2	Mass determination of the leptonic scalar ϕ	25
4	Discussions and conclusion	26
A	Feynman rules	28
B	The functions G and \mathcal{F}	28
C	One-loop RGEs	30
D	Analytical perturbativity limits	33
E	Unitarity limits	34

1 Introduction

Explanation of tiny but non-zero masses of neutrinos, as confirmed in various experiments over the past two decades [1], requires new physics beyond the Standard Model (SM). In addition to the origin of their masses and mixing, neutrinos pose many more unanswered questions. For example, we still do not know whether the neutrino masses are of Dirac-type or Majorana-type; see Ref. [2] for a recent review. We would also like to understand whether the neutrino sector contains new interactions beyond those allowed by the SM gauge structure, *i.e.* the so-called non-standard interactions (NSIs); see Ref. [3] for a recent status report. Just like neutrinos, the origin of dark matter (DM) is also a puzzle and it is conceivable that these two puzzles could be somehow correlated at a fundamental level

[4]. We also wonder whether the leptonic sector breaks CP-symmetry and whether it is responsible for the observed matter-antimatter asymmetry in the Universe [5]. In order to address these outstanding puzzles, construction of neutrino models and investigation of their predictions at various experiments are highly motivated.

If neutrinos are Majorana particles, lepton number L , which is an accidental global symmetry of the SM Lagrangian, must be broken either at tree-level or loop-level. On the other hand, if neutrinos are Dirac particles, lepton number (or some non-anomalous symmetry that contains L , such as $B - L$) remains a good symmetry of the Lagrangian. We will focus on this latter case, assuming that $B - L$ is conserved even in presence of higher-dimensional operators. Thus, any new, additional degrees of freedom must be charged appropriately under global $B - L$ [6]. In a recent paper [7], motivated by certain observational considerations at the LHC and beyond, we considered the possibility that Dirac neutrinos could exhibit NSIs with a new (light) scalar field ϕ which has a $B - L$ charge of $+2$ but is a singlet under the SM gauge group. These were dubbed as “leptonic scalars”, which can only couple to right-handed neutrinos (ν_R) (or left-handed anti-neutrinos) like $\nu_R^T C \nu_R \phi$ at the renormalizable level. Then the question arises as to how these leptonic scalars couple to the SM fields. At the dimension-6 level, we can write an effective coupling of the form

$$\frac{1}{\Lambda^2} (LH)(LH)\phi, \quad (1.1)$$

where L and H are the SM lepton and Higgs doublets, respectively, and Λ is the new physics scale. After electroweak (EW) symmetry breaking, the operator (1.1) yields flavor-dependent NSIs of neutrinos with the leptonic scalar of the form $\lambda_{\alpha\beta} \phi \nu_\alpha \nu_\beta$. Furthermore, at energy scales below the mass of ϕ , this leads to an effective non-standard neutrino self-interaction, which could have observable cosmological consequences [8–11].

Our goal in this paper is to find an ultraviolet (UV)-completion of the operator (1.1) and to test the model at the ongoing LHC and future 100 TeV colliders, such as the Future Circular Collider (FCC-hh) at CERN [12] and the Super Proton-Proton Collider (SPPC) in China [13]. To be concrete, we adopt a Type-II seesaw motivated neutrino mass model [14–19], where the neutral component of the triplet scalar field Δ does not acquire a vacuum expectation value (VEV) which keeps the custodial symmetry intact. The lepton number is not broken and the neutrinos are Dirac-type in this model. We also add a SM-singlet complex scalar field Φ , which gives rise to the leptonic scalar ϕ in the model. Beyond the NSIs between the active neutrinos and the leptonic scalar, the particle spectrum and new interactions in this model lead to rich phenomenology and consequently new observable signatures. In some other UV-complete models, the effective interactions of ϕ with the SM neutrinos stemming from Eq. (1.1) might also be relevant to DM phenomenology [20–22].

In this paper we will show that the distinguishing features of the signatures of our UV-complete model compared to the standard Type-II seesaw model is due to the new sources of missing energy carried away by ϕ , which would help the model to be detected at the ongoing LHC and future higher-energy colliders. After taking into account the current limits from the low-energy lepton flavor violating (LFV) constraints (cf. Table 2 and Fig. 2) and the theoretical limits from perturbativity and unitarity (see Fig. 3), we

consider two scenarios with respectively small and large Yukawa couplings of the leptonic scalar ϕ . In both these scenarios, ϕ can be produced either from the doubly-charged scalar $H^{\pm\pm} \rightarrow W^\pm W^\pm \phi$ or from the singly-charged scalar $H^\pm \rightarrow W^\pm \phi$ – channels which are unique and absent in the standard Type-II seesaw. As the leptonic scalar ϕ decays exclusively into neutrinos, these new channels will lead to same-sign dilepton plus missing transverse energy plus jets signal at the hadron colliders. Detailed cut-based analysis is carried out for both scenarios, and the technique of Boosted Decision Tree (BDT) [23] is also utilized to improve the observational significance (see Tables 4 and 6). We find that the mass of doubly-charged scalars in the small and large Yukawa coupling scenarios can be probed up to respectively 800 GeV and 1.1 TeV at the 2σ significance, corresponding to a 95% confidence level, in the new channels at the high-luminosity LHC (HL-LHC) with integrated luminosity of 3 ab^{-1} , and can be improved up to 3.8 TeV and 4 TeV respectively at future 100 TeV colliders with luminosity of 30 ab^{-1} . We also show that since in the large Yukawa coupling case, the missing energy is completely from the leptonic scalar, its mass can be determined with an accuracy of about 10% at the HL-LHC.

The rest of the paper is organized as follows. In Section 2, we present the model details and lay out relevant experimental and theoretical constraints, including the key parameters and resultant main decay channels of $H^{\pm\pm}$ and H^\pm in Section 2.1, the current low-energy LFV constraints on $H^{\pm\pm}$ in Section 2.2, and the high-energy limits from perturbativity and unitarity in Section 2.3. In Section 3, we discuss our search strategy at the LHC and future 100 TeV hadron colliders, presenting the small Yukawa coupling case in Section 3.1 and large Yukawa coupling scenario in Section 3.2. We show the discovery potential by utilizing the cut-based analysis and the BDT techniques, and obtain the prospect for determining the mass of ϕ in the large Yukawa coupling case even though the scalar ϕ escapes from the detectors as missing energy. The main results are summarized in Section 4. For the sake of completeness, the complete set of Feynman rules for the model are listed in Appendix A. The functions G and \mathcal{F} for some three-body decays are given in Appendix B. The renormalization group equations (RGEs) for the couplings are detailed in Appendix C. The perturbativity limits are analytically derived in Appendix D, and the unitarity limits are described in Appendix E.

2 The model

In this section, we present a global $(B - L)$ -conserved UV-complete model of a leptonic scalar, which is motivated by the well-known Type-II seesaw model [14–19]. The enlarged particle content of the model includes a leptonic complex scalar Φ , which is a singlet under the SM gauge groups and carries a $B - L$ charge of $+2$. The model contains also an $SU(2)_L$ triplet scalar Δ with hypercharge $+1$ and $B - L$ charge $+2$:

$$\Delta = \begin{pmatrix} \frac{1}{\sqrt{2}}\delta^+ & \delta^{++} \\ \delta^0 & -\frac{1}{\sqrt{2}}\delta^+ \end{pmatrix} \quad (2.1)$$

and three SM-singlet $B - L = -1$ right-handed neutrino fields ν_{R_i} ($i = 1, 2, 3$).

The allowed Yukawa interactions in the model are given by

$$-\mathcal{L}_Y = y_{\nu, \alpha\beta} \bar{L}_\alpha H \nu_{R\beta} + Y_{\alpha\beta} L_\alpha^\top C i \sigma_2 \Delta L_\beta + \tilde{y}_{\nu, \alpha\beta} \nu_{R\alpha}^\top C \nu_{R\beta} \Phi + \text{H.c.}, \quad (2.2)$$

where $\alpha, \beta = e, \mu, \tau$ are the lepton flavor indices, C is the charge-conjugation operator, σ_2 is the second Pauli matrix, y_ν are the SM-like Yukawa couplings of the neutrinos, $Y_{\alpha\beta}$ are the new leptonic Yukawa couplings of the triplet that govern the heavy scalar phenomenology, and \tilde{y}_ν are the Yukawa couplings of the leptonic scalar Φ to the right-handed neutrinos. In a $(B-L)$ -conserved theory where Δ and Φ do not acquire any VEV, neutrinos are Dirac fermions and non-zero neutrino masses can be generated after the EW symmetry breaking from the first term of the Yukawa Lagrangian given in Eq. (2.2), just like the other fermions in the SM. However, one requires $y_\nu \lesssim 10^{-12}$ in order to satisfy the absolute neutrino mass constraints [24, 25].

The kinetic and potential terms of the scalar sector are given by

$$\mathcal{L}_{\text{Scalar}} = (D_\mu H)^\dagger (D^\mu H) + \text{Tr}[(D_\mu \Delta)^\dagger (D^\mu \Delta)] + (\partial_\mu \Phi)^\dagger (\partial^\mu \Phi) - V(H, \Delta, \Phi), \quad (2.3)$$

where the covariant derivatives are given by

$$D_\mu H = \partial_\mu H - i \frac{g_L}{2} W_\mu^a \sigma_a H - i \frac{g_Y}{2} B_\mu H, \quad (2.4)$$

$$D_\mu \Delta = \partial_\mu \Delta - i \frac{g_L}{2} [W_\mu^a \sigma_a, \Delta] - i g_Y B_\mu \Delta, \quad (2.5)$$

with g_L and g_Y respectively the gauge couplings for the SM gauge groups $SU(2)_L$ and $U(1)_Y$, and σ_a ($a = 1, 2, 3$) the Pauli matrices. The most general renormalizable potential involving the scalar fields of the model is given by

$$\begin{aligned} V(H, \Delta, \Phi) = & -m_H^2 + \frac{\lambda}{4} (H^\dagger H)^2 + M_\Delta^2 \text{Tr}(\Delta^\dagger \Delta) + M_\Phi^2 \Phi^\dagger \Phi \\ & + \lambda_1 (H^\dagger H) \text{Tr}(\Delta^\dagger \Delta) + \lambda_2 [\text{Tr}(\Delta^\dagger \Delta)]^2 + \lambda_3 \text{Tr}[(\Delta^\dagger \Delta)^2] + \lambda_4 (H^\dagger \Delta) (\Delta^\dagger H) \\ & + \lambda_5 (\Phi^\dagger \Phi)^2 + \lambda_6 (\Phi^\dagger \Phi) (H^\dagger H) + \lambda_7 (\Phi^\dagger \Phi) \text{Tr}(\Delta^\dagger \Delta) \\ & + \lambda_8 (i \Phi H^\top \sigma_2 \Delta^\dagger H + \text{H.c.}), \end{aligned} \quad (2.6)$$

where all the mass parameters m_H^2 , M_Δ^2 , M_Φ^2 and the quartic couplings λ and λ_i are assumed to be real. The scalar Δ in our model carries the same $SU(3)_C \times SU(2)_L \times U(1)_Y$ charges $(\mathbf{1}, \mathbf{3}, 1)$ as in the Type-II seesaw model. However, the presence of a $(B-L)$ -charged Φ and the $B-L$ conservation in our model have important phenomenological consequences associated with the triplet Δ , which is different from that in the Type-II seesaw scenario. In the Type-II seesaw model, the EW symmetry breaking induces a non-vanishing VEV for the triplet Δ via the cubic term $H^\top i \sigma_2 \Delta^\dagger H$. However, due to the $B-L$ conservation such a cubic term does not exist in our model, and as a result the triplet Δ does not develop a VEV in our model. As we will see in Section 3, this leads to very interesting signatures at the LHC and future 100 TeV colliders, which are key to distinguish our model from the Type-II seesaw.

After the EW symmetry breaking, the Higgs doublet H develops a VEV $v = (\sqrt{2} G_F)^{-1/2}$ with G_F being the Fermi constant, and the mass matrix of the CP-even neutral components

in the $\{h, \delta^{0r}, \Phi^r\}$ basis (here X^r refers to the real component of the field X) is

$$M_{\text{CP-even}}^2 = \begin{pmatrix} \frac{1}{2}\lambda v^2 & 0 & 0 \\ 0 & M_\Delta^2 + \frac{1}{2}(\lambda_1 + \lambda_4)v^2 & -\frac{1}{2}\lambda_8 v^2 \\ 0 & -\frac{1}{2}\lambda_8 v^2 & M_\Phi^2 + \frac{1}{2}\lambda_6 v^2 \end{pmatrix}. \quad (2.7)$$

As the singlet and triplet scalars do not have VEVs, the component h from the SM doublet H does not mix with other neutral scalars, as can be seen from Eq. (2.7). Then h can be readily identified as the 125 GeV Higgs boson observed at the LHC [26, 27], and the quartic coupling λ can be identified as the SM quartic coupling. The two remaining physical CP-even scalar eigenstates are from mixing of the components Φ^r and δ^{0r} of the leptonic fields Φ and Δ with $B - L$ charge of $+2$, and thus are both physical leptonic scalars. Denoting H_1 as the lighter one and H_2 as the heavier one, they can be obtained by the following rotation

$$\begin{pmatrix} H_1 \\ H_2 \end{pmatrix} = \begin{pmatrix} \cos \theta & -\sin \theta \\ \sin \theta & \cos \theta \end{pmatrix} \begin{pmatrix} \Phi^r \\ \delta^{0r} \end{pmatrix}, \quad (2.8)$$

where the mixing angle θ is given by

$$\tan 2\theta = \frac{\lambda_8 v^2}{M_\Delta^2 + v^2(\lambda_1 + \lambda_4 - \lambda_6)/2 - M_\Phi^2}, \quad (2.9)$$

and the two eigenvalue masses are

$$M_{H_{1,2}}^2 = \frac{1}{2} (M_\Delta^2 + M_\Phi^2) + \frac{1}{4}(\lambda_1 + \lambda_4 + \lambda_6)v^2 \mp \frac{1}{4} \sqrt{[2M_\Delta^2 - 2M_\Phi^2 + (\lambda_1 + \lambda_4 - \lambda_6)v^2]^2 + 4\lambda_8^2 v_H^4}. \quad (2.10)$$

Similarly, the two CP-odd leptonic scalars (A_1, A_2) from the imaginary components Φ^i, δ^{0i} have exactly the same masses as the CP-even scalars, *i.e.*

$$M_{A_1} = M_{H_1}, \quad M_{A_2} = M_{H_2}. \quad (2.11)$$

For the sake of illustration, we choose to work in the regime where the leptonic scalars (A_1, H_1) are in the mass range $M_h/2 < M_{H_1, A_1} \lesssim \mathcal{O}(100)$ GeV. The lower mass bound is to avoid the invisible decay of the SM Higgs $h \rightarrow H_1 H_1$, $A_1 A_1 \rightarrow \nu \nu \bar{\nu} \bar{\nu}$, while the upper bound is mainly motivated from our previous collider study [7], where the sensitivity in the vector boson fusion (VBF) channel was found to drop exponentially beyond 100 GeV or so. In order to keep the two leptonic scalars (A_1, H_1) light, we choose the simplest scenario $\lambda_6 = 0$. There is also a pair of heavy leptonic scalars H_2 and A_2 , which can either decay into neutrinos or cascade decay into gauge bosons and lighter scalars. For simplicity, we just assume (H_2, A_2) to be heavier than the EW scale such that they are not relevant for our consideration here, and a detailed collider study of their phenomenology is deferred to future work. Finally, it is trivial to get the masses of the singly- and doubly-charged scalars, which are respectively given by

$$M_{H^\pm}^2 = M_\Delta^2 + \frac{1}{4}(2\lambda_1 + \lambda_4)v^2, \quad (2.12)$$

Table 1. Important couplings for the neutral scalars H_1 , A_1 , the singly-charged scalar H^\pm and the doubly-charged scalar $H^{\pm\pm}$. Here e is the electric charge, $s_W \equiv \sin \theta_W$ and $c_W \equiv \cos \theta_W$ the sine and cosine of the Weinberg angle θ_W , $p_{1,2}$ the momenta for the first and second particles in the vertices, and $P_L = \frac{1}{2}(1 - \gamma_5)$ the left-handed projection operator. See Appendix. A for the full set of Feynman rules.

Vertices	Couplings
$H_1 \nu_\alpha \nu_\beta$	$-i \sqrt{2} Y_{\alpha\beta} \sin \theta P_L$
$A_1 \nu_\alpha \nu_\beta$	$\sqrt{2} Y_{\alpha\beta} \sin \theta P_L$
$H^+ H^- \gamma_\mu$	$i e (p_1 - p_2)_\mu$
$H^+ H^- Z_\mu$	$-i e \frac{s_W}{c_W} (p_1 - p_2)_\mu$
$H^+ \ell_\alpha^- \nu_\beta$	$\sqrt{2} i Y_{\alpha\beta} P_L$
$H^+ H_1 W_\mu^-$	$i \frac{g_L}{\sqrt{2}} (p_1 - p_2)_\mu \sin \theta$
$H^+ A_1 W_\mu^-$	$\frac{g_L}{\sqrt{2}} (p_1 - p_2)_\mu \sin \theta$
$H^{++} H^{--} \gamma_\mu$	$2i e (p_1 - p_2)_\mu$
$H^{++} H^{--} Z_\mu$	$i e \frac{c_W^2 - s_W^2}{c_W s_W} (p_1 - p_2)_\mu$
$H^{++} \ell_\alpha^- \ell_\beta^-$	$2i Y_{\alpha\beta} P_L$
$H^{++} H^- W_\mu^-$	$-i g_L (p_1 - p_2)_\mu$
$H^{++} W_\mu^- W_\nu^- H_1$	$-i \sqrt{2} g_L^2 \sin \theta g_{\mu\nu}$
$H^{++} W_\mu^- W_\nu^- A_1$	$-\sqrt{2} g_L^2 \sin \theta g_{\mu\nu}$

$$M_{H^{\pm\pm}}^2 = M_\Delta^2 + \frac{1}{2} \lambda_1 v^2. \quad (2.13)$$

Depending on the sign of λ_4 , H^\pm can be lighter or heavier than $H^{\pm\pm}$.

2.1 Key parameters and decay channels of $H^{\pm\pm}$ and H^\pm

The interactions of the new scalars with the SM fields are generated through the gauge couplings in Eqs. (2.4) and (2.5), the scalar couplings in Eq. (2.6) and the Yukawa interactions in Eq. (2.2) including potential scalar mixing in Eq. (2.8). All the key interactions of the neutral scalars H_1 , A_1 , the singly-charged scalar H^\pm and the doubly-charged scalar $H^{\pm\pm}$ for the hadron collider analysis below are collected in Table 1. For the sake of completeness, we have listed the complete set of Feynman rules in Tables 7 to 11 in Appendix A.

The gauge interactions of H^\pm and $H^{\pm\pm}$ with the SM photon, W and Z bosons in Table 1 are relevant for the pair production $H^{++} H^{--}$ and the associated production $H^{\pm\pm} H^\mp$ of the doubly-charged scalar at hadron colliders, as in the Type-II seesaw case [28–45]. The remaining couplings in Table 1 are relevant to the decays of H^\pm and $H^{\pm\pm}$. For the singly-charged scalar H^\pm , besides the leptonic final states, it can decay into a light neutral scalar H_1 or A_1 and a W boson, which is absent in the Type-II seesaw model. The corresponding partial decay widths are respectively

$$\Gamma(H^\pm \rightarrow l_\alpha^\pm \nu_\beta) = \frac{Y_{\alpha\beta}^2 M_{H^\pm}}{8\pi}, \quad (2.14)$$

$$\Gamma(H^\pm \rightarrow W^\pm H_1) = \Gamma(H^\pm \rightarrow W^\pm A_1) = \frac{G_F \sin^2 \theta M_{H^\pm}^3}{4\sqrt{2}\pi} \lambda^{3/2} \left(\frac{M_W^2}{M_{H^\pm}^2}, \frac{M_{H_1}^2}{M_{H^\pm}^2} \right), \quad (2.15)$$

where the function

$$\lambda(x, y) \equiv 1 + x^2 + y^2 - 2xy - 2x - 2y. \quad (2.16)$$

As in the standard Type-II seesaw, the singly-charged scalar H^\pm can decay into a heavy scalar H_2 or A_2 and a W boson. However, the mass splitting between the triplet scalar components is severely constrained by the EW precision data (EWPT), in terms of the oblique S and T parameters [46, 47]: depending on the triplet scalar masses, it is required that the mass splitting $\Delta M \lesssim 50$ GeV [34, 42, 48, 49]. Therefore the W boson is always off-shell, *i.e.* $H^\pm \rightarrow W^{\pm*} H_2, W^{\pm*} A_2$ (the corresponding interaction can be found in Table 9), and the corresponding widths are given by

$$\Gamma(H^\pm \rightarrow W^{\pm*} H_2) = \Gamma(H^\pm \rightarrow W^{\pm*} A_2) = \frac{9g_L^4 \cos^2 \theta M_{H^\pm}}{256\pi^3} G \left(\frac{M_{H_2}^2}{M_{H^\pm}^2}, \frac{M_W^2}{M_{H^\pm}^2} \right), \quad (2.17)$$

where the function $G(x, y)$ is explicitly given in Appendix B. This channel is highly suppressed by the off-shell W^* boson, and will be neglected in the following sections.

In our model, the doubly-charged scalar $H^{\pm\pm}$ can decay into same-sign dilepton pairs and the three-body final state $W^\pm W^\pm H_1$ and $W^\pm W^\pm A_1$. The partial widths are given respectively by

$$\Gamma(H^{\pm\pm} \rightarrow l_\alpha^\pm l_\alpha^\pm) = \frac{S_{\alpha\beta} Y_{\alpha\beta}^2 M_{H^{\pm\pm}}}{4\pi}, \quad (2.18)$$

$$\Gamma(H^{\pm\pm} \rightarrow W^\pm W^\pm H_1) = \Gamma(H^{\pm\pm} \rightarrow W^\pm W^\pm A_1) = \frac{g_L^4 \sin^2 \theta}{512\pi^3 M_{H^{\pm\pm}}^3} \int \mathcal{F} dm_{12}^2 dm_{23}^2, \quad (2.19)$$

where $S_{\alpha\beta} = 1/2$ (1) for $\alpha \neq \beta$ ($\alpha = \beta$) is a symmetry factor, and the dimensionless lengthy function \mathcal{F} is put in Appendix B, which is a function of m_{12}^2 and m_{23}^2 . The phase space is integrated over the Dalitz plot where the ranges for m_{12}^2 and m_{23}^2 are respectively $[4M_W^2, (M_{H^{\pm\pm}} - M_{H_1})^2]$ and $[(M_W + M_{H_1})^2, (M_{H^{\pm\pm}} - M_W)^2]$. There is also a two-body bosonic channel, with the partial width

$$\Gamma(H^{\pm\pm} \rightarrow W^{\pm*} H^\pm) = \frac{9g_L^4 M_{H^{\pm\pm}}}{128\pi^3} G \left(\frac{M_{H^\pm}^2}{M_{H^{\pm\pm}}^2}, \frac{M_W^2}{M_{H^{\pm\pm}}^2} \right). \quad (2.20)$$

with the function $G(x, y)$ defined in Appendix B. As for the singly-charged scalar in Eq. (2.17), this channel is highly suppressed by the off-shell W boson, and will be neglected in the following analysis. Since the masses and decay properties of H_1 and A_1 are the same in our model, we henceforth collectively use ϕ to denote both the leptonic scalars H_1 and A_1 , *i.e.* $\phi = H_1, A_1$.

In the standard Type-II seesaw, there is also the cascade decay channel for the doubly-charged scalar [31, 34]:

$$H^{\pm\pm} \rightarrow H^\pm W^{\pm*} \rightarrow H_2 W^{\pm*} W^{\pm*}. \quad (2.21)$$

In a large region of parameter space, the dilepton channels $H^{\pm\pm} \rightarrow \ell^\pm \ell^\pm$ and diboson channel $H^{\pm\pm} \rightarrow W^\pm W^\pm$ are highly suppressed respectively by the small Yukawa couplings $Y_{\alpha\beta}$ and the small VEV v_Δ of the triplet, and the doubly-charged scalar $H^{\pm\pm}$ decays mostly via the cascade channel above. When the mixing of H_2 with the SM Higgs is small, the neutral scalar H_2 decays mostly further into neutrinos via the Yukawa coupling $Y_{\alpha\beta}$. If the cascade channel dominates, the current direct LHC constraints on $M_{H^{\pm\pm}}$ in the $\ell^\pm \ell^\pm$ [50, 51] and $W^\pm W^\pm$ [52, 53] channels will be largely weakened. Then a relatively light $H^{\pm\pm}$ implies that the neutral scalar H_2 may also be light. This makes the decay channel of (2.21) in the standard Type-II seesaw to some extent similar to our case in Eq. (2.19), both leading to the signal of same-sign dilepton plus missing transverse energy (assuming W boson decaying leptonically). However, as a result of the severe EWPT constraint on the mass splitting ΔM of the triplet scalars [34, 42, 48, 49], the two W bosons are both off-shell in the cascade decay in Eq. (2.21), which is very different from the on-shell W bosons in Eq (2.19) in our case.

Similarly, in the standard Type-II seesaw model the singly-charged scalar H^\pm can decay into $\ell^\pm \nu$ and hW^\pm , ZW^\pm , $t\bar{b}$, which are respectively proportional to the couplings $Y_{\alpha\beta}$ and v_Δ [31]. When both $Y_{\alpha\beta}$ and v_Δ are relatively small, the decay of H^\pm will be dominated by

$$H^\pm \rightarrow H_2 W^{\pm*}, \quad (2.22)$$

where the W boson is again off-shell as a result of the EWPT limit on the triplet scalar mass splitting. As in the doubly-charged scalar case, the decay $H^\pm \rightarrow H_2 W^{\pm*}$ with a light H_2 in the Type-II seesaw is very similar to the channel $H^\pm \rightarrow W^\pm \phi$ in our model, except for the off-shell W boson.

Therefore, the new decay channels $H^{\pm\pm} \rightarrow W^\pm W^\pm \phi$ and $H^\pm \rightarrow W^\pm \phi$ make our model very different from the standard Type-II seesaw in the following aspects, which can be used to distinguish the two models at the high-energy colliders:

- The $W^\pm W^\pm \phi$ final state from the $H^{\pm\pm}$ decay is absent in the standard Type-II seesaw model, where the W bosons in the decays in Eqs. (2.19) and (2.22) are off-shell.
- Another distinguishing feature of this model is that the decays $H^{\pm\pm} \rightarrow W^\pm W^\pm \phi$ and $H^\pm \rightarrow W^\pm \phi$ does not necessarily correspond to the compressed mass gaps among different particle states of the triplet Δ , whereas in the standard Type-II seesaw model the decays in Eqs. (2.19) and (2.22) are very sensitive to the mass splitting ΔM of the triplet scalars.

Depending on the value of the Yukawa couplings $Y_{\alpha\beta}$, there are two distinct scenarios for the decays of $H^{\pm\pm}$ and H^\pm :

- Large Yukawa coupling scenario with $Y_{\alpha\beta} \sim \mathcal{O}(1)$. In this case the leptonic channels $H^{\pm\pm} \rightarrow \ell^\pm \ell^\pm$ and $H^\pm \rightarrow \ell^\pm \nu$ dominate, which are from the Yukawa interactions $Y_{\alpha\beta}$.

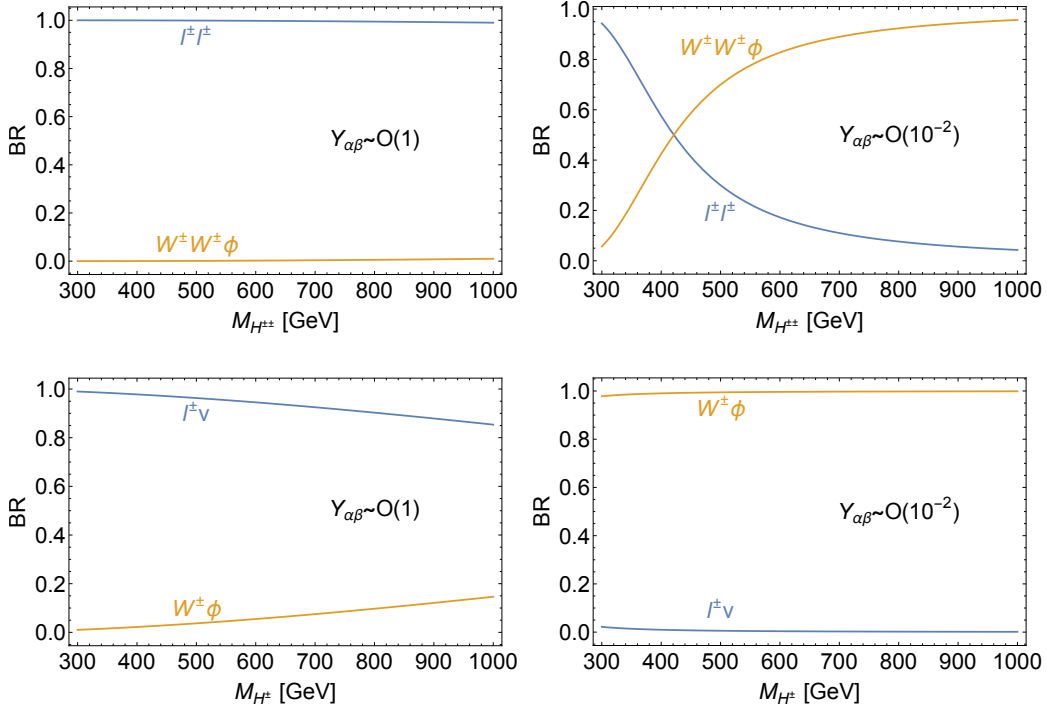


Figure 1. Branching fractions of $H^{\pm\pm}$ decay (upper panels) and H^\pm decay (lower panels) as a function of their masses. The left and right panels are for the large and small Yukawa coupling scenarios, respectively. Here ϕ denotes a leptonic scalar H_1/A_1 .

- Small Yukawa coupling scenario with $Y_{\alpha\beta} \lesssim \mathcal{O}(10^{-2})$. In this case the bosonic channels $H^{\pm\pm} \rightarrow W^\pm W^\pm \phi$ and $H^\pm \rightarrow W^\pm \phi$ dominate, which originate from the gauge couplings in Eqs. (2.4) and (2.5).

For simplicity, we will not consider the intermediate scenarios, where the branching fractions (BRs) of bosonic and fermionic decay channels above are comparable. The W -dominated final states for small Yukawa couplings $Y_{\alpha\beta}$ depend on the scalar mixing angle $\sin\theta$, which in turn depends on λ_8 as shown in Eq. (2.9), where we find that λ_8 needs to be $\mathcal{O}(1)$ in order to have a sizable $\sin\theta$. The decay branching fractions of $H^{\pm\pm}$ and H^\pm are shown respectively in the upper and lower panels of Fig. 1 as a function of their masses. The left and right panels are respectively for the large and small Yukawa coupling scenarios. As shown in the bottom left panel, if the Yukawa couplings are of order one, the dominant decay channels of H^\pm will be $\ell^\pm \nu$, but the bosonic channel $W^\pm \phi$ is still feasible in the high mass regime with a branching fraction around 10%. For small Yukawa couplings of order $\mathcal{O}(10^{-2})$, the singly-charged scalar H^\pm decays predominantly into $W^\pm \phi$, as demonstrated in the bottom right panel. On the other hand, as shown in the top left panel, the doubly-charged scalar $H^{\pm\pm}$ will decay mostly to $\ell^\pm \ell^\pm$ if the Yukawa couplings are large, while the $W^\pm W^\pm \phi$ channel is dominant for small Yukawa couplings although a crossover happens for low $M_{H^{\pm\pm}}$, as shown in the top right panel.

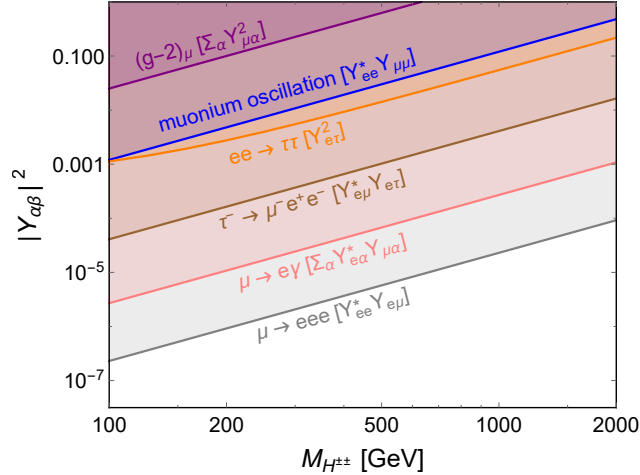


Figure 2. LFV limits on the Yukawa couplings $|Y_{\alpha\beta}|^2$ as a function of the doubly-charged scalar mass $M_{H^{\pm\pm}}$. The shaded regions are excluded. See text and Table 2 for more details.

2.2 Low-energy LFV constraints

There exist numerous constraints on the charged Higgs sector from the low-energy flavor data, such as those from the LFV decays $\ell_\alpha \rightarrow \ell_\beta \ell_\gamma \ell_\delta$, $\ell_\alpha \rightarrow \ell_\beta \gamma$ [1, 54], anomalous electron [55] and muon [56, 57] magnetic moments, muonium oscillation [58], and the LEP $e^+e^- \rightarrow \ell^+\ell^-$ data [59]. Following Ref. [39], the updated LFV limits on the Yukawa couplings $Y_{\alpha\beta}$ are collected in Table 2, and the most stringent ones are shown in Fig. 2, as a function of the doubly-charged scalar mass $M_{H^{\pm\pm}}$. We see that the products involving two flavor transitions are highly constrained, while the bounds on an individual coupling are much weaker, especially for the tau flavor.

It should be noted that the contributions of $H^{\pm\pm}$ to the electron and muon $g-2$ are always negative [60]. Therefore, the recent measurement of muon $g-2$ at Fermilab [57] cannot be interpreted as the effect of $H^{\pm\pm}$ in our model. On the other hand, we can use the reported measurement of Ref. [57]

$$\Delta a_\mu = a_\mu^{\text{exp}} - a_\mu^{\text{SM}} = (251 \pm 59) \times 10^{-11}, \quad (2.23)$$

which is 4.2σ larger than the SM prediction [61], to set limits on the $H^{\pm\pm}$ parameter space. We will use a conservative 5σ bound, *i.e.* require that the magnitude of the new contribution to $(g-2)_\mu$ from $H^{\pm\pm}$ must not exceed $0.8 \times 59 \times 10^{-11}$. The corresponding limit on the Yukawa coupling $Y_{\mu\beta}$ is shown by the purple shaded region in Fig. 2 and also in Table 2. Note that if a light scalar has an LFV coupling $h_{\mu\tau}$ to muon and tau, it could be a viable candidate to explain the muon $g-2$ anomaly, while satisfying all current constraints [62–68]. Such neutral scalar interpretations of muon $g-2$ anomaly can be definitively tested at a future muon collider [69–73].

2.3 High-energy behavior: perturbativity and unitarity limits

Since larger values of λ_8 and $Y_{\alpha\beta}$ play important roles for the hadron collider signal of this model, let us first check the largest values of these couplings which can be accommodated

Table 2. Upper limits on the Yukawa couplings $|Y_{\alpha\beta}|^2$ (or $|Y_{\alpha\gamma}^\dagger Y_{\beta\gamma}|$) from the current experimental limits on the LFV branching fractions of $l_\alpha \rightarrow l_\beta l_\gamma l_\delta$, $l_\alpha \rightarrow l_\beta \gamma$ [1, 54], anomalous electron [55] and muon [56, 57] magnetic moments, muonium oscillation [58], and LEP $e^+e^- \rightarrow l^+l^-$ data [59]. See also Fig. 2.

Process	Experimental bound	Constraint $\times \left(\frac{M_{H^{\pm\pm}}}{100 \text{ GeV}}\right)^2$
$\mu^- \rightarrow e^- e^+ e^-$	$< 1.0 \times 10^{-12}$	$ Y_{ee}^\dagger Y_{e\mu} < 2.3 \times 10^{-7}$
$\tau^- \rightarrow e^- e^+ e^-$	$< 1.4 \times 10^{-8}$	$ Y_{ee}^\dagger Y_{e\tau} < 6.5 \times 10^{-5}$
$\tau^- \rightarrow e^- \mu^+ \mu^-$	$< 1.6 \times 10^{-8}$	$ Y_{e\mu}^\dagger Y_{\mu\tau} < 4.9 \times 10^{-5}$
$\tau^- \rightarrow \mu^- e^+ \mu^-$	$< 9.8 \times 10^{-9}$	$ Y_{e\tau}^\dagger Y_{\mu\mu} < 5.5 \times 10^{-5}$
$\tau^- \rightarrow \mu^- e^+ e^-$	$< 1.1 \times 10^{-8}$	$ Y_{e\mu}^\dagger Y_{e\tau} < 4.1 \times 10^{-5}$
$\tau^- \rightarrow e^- \mu^+ e^-$	$< 8.4 \times 10^{-9}$	$ Y_{ee}^\dagger Y_{\mu\tau} < 5.1 \times 10^{-5}$
$\tau^- \rightarrow \mu^- \mu^+ \mu^-$	$< 1.2 \times 10^{-8}$	$ Y_{\mu\mu}^\dagger Y_{\mu\tau} < 6.1 \times 10^{-5}$
$\mu^- \rightarrow e^- \gamma$	$< 4.2 \times 10^{-13}$	$ \sum_\gamma Y_{e\gamma}^\dagger Y_{\mu\gamma} < 2.7 \times 10^{-6}$
$\tau^- \rightarrow e^- \gamma$	$< 3.3 \times 10^{-8}$	$ \sum_\gamma Y_{e\gamma}^\dagger Y_{\tau\gamma} < 1.8 \times 10^{-3}$
$\tau^- \rightarrow \mu^- \gamma$	$< 4.4 \times 10^{-8}$	$ \sum_\gamma Y_{\mu\gamma}^\dagger Y_{\tau\gamma} < 2.1 \times 10^{-3}$
electron $g-2$	$< 5.2 \times 10^{-13}$	$\sum_\beta Y_{e\beta} ^2 < 1.2$
muon $g-2$	$< 4.7 \times 10^{-10}$	$\sum_\beta Y_{\mu\beta} ^2 < 0.025$
muonium oscillation	$< 8.2 \times 10^{-11}$	$ Y_{ee}^\dagger Y_{\mu\mu} < 0.0012$
$e^+e^- \rightarrow e^+e^-$	$\Lambda_{\text{eff}} > 5.2 \text{ TeV}$	$ Y_{ee} ^2 < 0.0012$
$e^+e^- \rightarrow \mu^+\mu^-$	$\Lambda_{\text{eff}} > 7.0 \text{ TeV}$	$ Y_{e\mu} ^2 < 6.4 \times 10^{-4}$
$e^+e^- \rightarrow \tau^+\tau^-$	$\Lambda_{\text{eff}} > 7.6 \text{ TeV}$	$ Y_{e\tau} ^2 < 5.4 \times 10^{-4}$

at the EW scale without becoming non-perturbative at a higher energy scale. For the purpose of illustration, we set just one Yukawa coupling $Y_{\mu\mu}$ to be non-vanishing, with all other Yukawa couplings $Y_{\alpha\beta}$ ($\alpha\beta \neq \mu\mu$) to be zero. This choice is compatible with the current limits in Table 2, as the products of the Yukawa couplings must be small due to the existing LFV limits, while a single coupling ($Y_{\mu\mu}$ in our case) can be as large as $Y_{\mu\mu} \sim \mathcal{O}(1)$ for $M_{H^{\pm\pm}} \sim 1 \text{ TeV}$.

To implement the perturbativity limits from the high-energy scale, we use the RGEs in Appendix C for all the gauge, scalar and Yukawa couplings given in Eqs. (2.4), (2.5), (2.2) and (2.6). From the RGEs, we find that λ_8 depends on $Y_{\mu\mu}$ at one-loop level, since both λ_8 and $Y_{\mu\mu}$ are associated with the interaction terms which involve the triplet scalars. The dependence of perturbativity limits on λ_8 on the Yukawa coupling $Y_{\mu\mu}(v)$ at the EW scale is shown in the left panel of Fig. 3, with perturbativity up to Planck scale M_{Pl} and the grand unified theory (GUT) scale M_{GUT} for the purple and red lines, and up to the 100 TeV and 10 TeV scales for the orange and pink lines, respectively. Comparing these lines, we can see that the perturbativity limits on λ_8 are very sensitive to the value of $Y_{\mu\mu}$ at the EW scale. To have a perturbative λ_8 at the 10 TeV (100 TeV) scale, it is required that the coupling $Y_{\mu\mu}(v) \lesssim 1.6$ (1.3). For a perturbative theory up to the GUT or Planck scale, the coupling $Y_{\mu\mu}$ needs to be even smaller, *i.e.* $Y_{\mu\mu}(v) \lesssim 0.68$. The perturbativity limits on λ_8 and $Y_{\mu\mu}$ at the EW scale as function of the scale $10 \text{ TeV} < \mu < M_{\text{Pl}}$ are shown in the right panel of Fig. 2. For the quartic coupling λ_8 , the solid and dashed lines

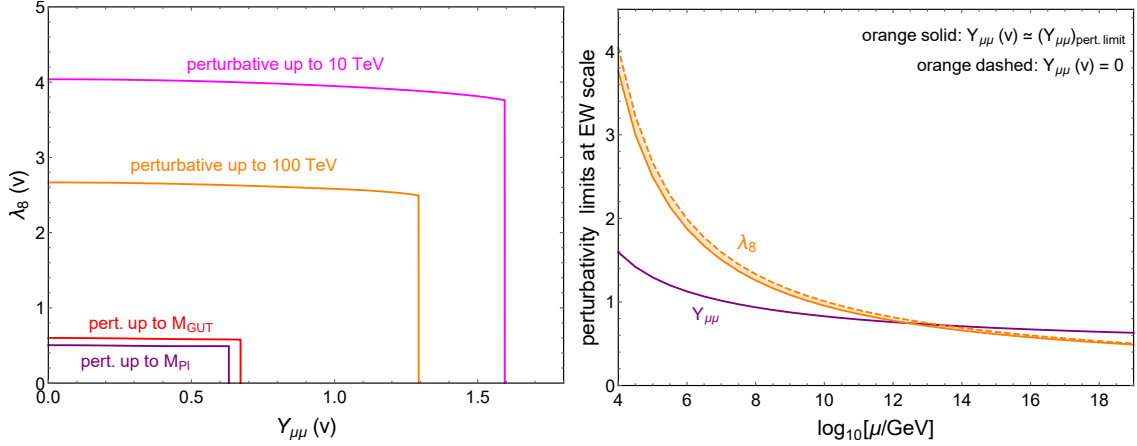


Figure 3. *Left panel:* Perturbativity limits on $\lambda_8(v)$ by the Landau pole at a higher scale of 10 TeV (magenta), 100 TeV (orange), the GUT scale (red) and the Planck scale (purple), as function of $Y_{\mu\mu}(v)$. *Right panel:* Perturbativity limits on λ_8 (orange) and $Y_{\mu\mu}$ (purple) at the EW scale, as function of the Landau pole scale μ . For the solid and dashed orange lines, we take $Y_{\mu\mu}$ to be respectively the perturbativity limit and zero at the EW scale.

correspond respectively to the cases of $Y_{\mu\mu}$ set at the perturbativity limit and $Y_{\mu\mu} = 0$ at the EW scale. As shown in both the two panels of Fig. 2, the quartic coupling λ_8 can be as large as 4 (2.6), with perturbativity holding up to 10 TeV (100 TeV). With the requirement of perturbativity up to the Planck (GUT) scale, we have $\lambda_8 \lesssim 0.5$ (0.6) at the EW scale.

The high-energy behavior of λ_8 , $Y_{\mu\mu}$ and other couplings can be understood analytically from the solutions of RGEs for these couplings. As a rough approximation, let us first see the analytical solution of $Y_{\mu\mu}$ without including the contributions from the gauge couplings $g_{S,L,Y}$ for the $SU(3)_C, SU(2)_L, U(1)_Y$ respectively. Defining $\alpha_\mu \equiv Y_{\mu\mu}^2/4\pi$, it is trivial to get the analytical solution of α_μ at scale μ from Eq. (C.14) as

$$\alpha_\mu(\mu) = \frac{\alpha_\mu(v)}{1 - \frac{4}{\pi}\alpha_\mu(v)t}, \quad \text{with} \quad t = \ln \frac{\mu}{v}. \quad (2.24)$$

It is clear from the above equation that the coupling $Y_{\mu\mu}$ is not asymptotically free and will blow up when the scale parameter approaches the value of

$$t_c = \ln \left(\frac{\mu_c}{v} \right) = \frac{\pi^2}{Y_{\mu\mu}^2(v)}. \quad (2.25)$$

With an initial value of $Y_{\mu\mu}(v) = 1.5$ at the EW scale, we can get the critical value of $t_c \simeq 4.39$, which corresponds to an energy scale of $\mu \simeq 20$ TeV. The full analytic solution of $Y_{\mu\mu}$ including the gauge coupling contributions is shown in Appendix D. Following the running of gauge couplings, and taking $g_L(M_Z) = 0.65100$, $g_Y(M_Z) = 0.357254$ (with M_Z the Z boson mass) [74–78], we find that in this case $t_c = 4.67$, which corresponds to $\mu \simeq 26$ TeV.

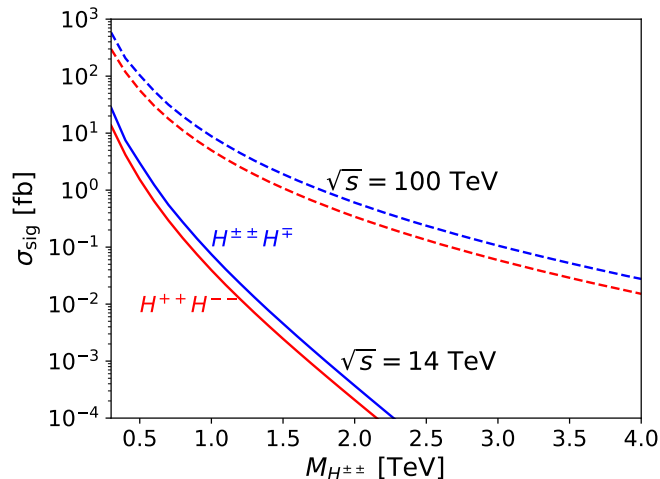


Figure 4. Cross sections of $H^{++}H^{--}$ pair (red) and $H^{\pm\pm}H^{\mp}$ associated (blue) production of doubly-charged scalars at $\sqrt{s} = 14$ TeV (solid) and $\sqrt{s} = 100$ TeV (dashed) pp colliders.

The contribution of $Y_{\mu\mu}$ to the evolution of λ_8 can be obtained from the following analytical solution of the RGE for λ_8 (see Appendix D for more details)

$$\lambda_8(\mu) = \lambda_8(v) \exp \left[\frac{1}{4\pi^2} \int_v^\mu E_8(\mu) d\mu \right], \quad (2.26)$$

where E_8 depends on $Y_{\mu\mu}$ as well as the couplings $g_{L,Y}$ and the top-quark Yukawa coupling y_t and is given in Eq. (D.12). As soon as $Y_{\mu\mu}$ turns non-perturbative, the exponential becomes very large and λ_8 also becomes non-perturbative.

We have also checked the unitarity constraints on $Y_{\mu\mu}$ and λ_8 , and the details are given in Appendix E. It is found that the unitarity constraints are much weaker $\lambda_8 < 10.0$, compared to the perturbativity constraints obtained here.

3 Collider signatures

In this section we analyze the striking signatures of this model at the LHC and future 100 TeV hadron colliders. We consider both the pair production and the associated production channels:

$$pp \rightarrow H^{++}H^{--}, H^{\pm\pm}H^{\mp}. \quad (3.1)$$

The production cross sections in the two channels for the doubly-charged scalar coming from an $SU(2)_L$ -triplet Δ at the 14 TeV LHC and future 100 TeV colliders have been estimated in Refs. [40, 79], which are reproduced in Fig. 4. As shown in Section 2.1, the final states associated with these production processes depend on the decay branching fractions of $H^{\pm\pm}$ and H^{\pm} . Our model predicts novel decay processes

$$H^{\pm\pm} \rightarrow W^{\pm}W^{\pm}\phi \quad \text{and} \quad H^{\mp} \rightarrow W^{\mp}\phi, \quad (3.2)$$

where the light leptonic scalars $\phi = H_1, A_1$ will escape from detection and lead to missing momentum. This can be used to distinguish our model from the standard Type-II seesaw. In this paper, we will focus on these novel channels. The prospects of the small Yukawa coupling scenario at future hadron colliders are investigated in Section 3.1, and the large Yukawa coupling case is analyzed in Section 3.2.

3.1 Small Yukawa coupling scenario

One typical choice of parameter is that the Yukawa coupling $Y_{\alpha\beta} \lesssim 10^{-2}$ to satisfy all the low-energy experimental limits in Section 2.2. Note that this choice of $Y_{\alpha\beta}$ would result in an effective $\nu_\alpha\nu_\beta\phi$ coupling $\lambda_{\alpha\beta}$ of order 10^{-3} , which is too small to probe in the VBF channel discussed in Ref. [7], but accessible in our UV-complete model due to the additional interactions, as shown below. In particular, under this choice of small Yukawa coupling, the doubly-charged scalar $H^{\pm\pm}$ will mostly decay to two W bosons and a light neutral leptonic scalar $\phi = H_1, A_1$; cf. the top right panel of Fig. 1. With two same-sign W bosons decaying leptonically and the other two decaying hadronically, the final state of our signal features two same-sign leptons (e or μ) plus jets and large missing transverse momentum in the pair production channel, *i.e.*

$$pp \rightarrow H^{++}(\rightarrow W^+W^+\phi) H^{--}(\rightarrow W^-W^-\phi) \rightarrow \ell^\pm\ell^\pm + 4 \text{ jets} + E_T^{\text{miss}}.$$

Similarly, we also have the associated production $pp \rightarrow H^{\pm\pm}H^\mp$ with $H^\mp \rightarrow W^\mp\phi$ which also has the same final states. However, due to the presence of less number of W 's, the contribution from the associated production is small to our signal.

We use `FeynRules` [80] to define the fields and the Lagrangian of our model, then the resulting UFO model file is fed into `MadGraph5_aMC@NLO` [81] to generate the Monte Carlo events where the decay of vector bosons is achieved by the `Madspin` [82] module integrated within `MadGraph5`. Next-to-leading order corrections are included by a k -factor of 1.25 [83] for our signal process. The leading SM backgrounds come from WZ and WW productions and the sub-leading ones from WWW and $t\bar{t}W$ processes are also considered. We use `MadGraph5` to generate the background events, and the leading ones are generated with two extra jets to properly account for the jet multiplicity in the final states. The events from the hard processes are showered with `Pythia8` [84] and the jets are clustered using `Fastjet` [85] with the anti- k_T algorithm [86] and the cone radius $\Delta R = 0.4$. All the signal and background events are smeared to simulate the detector effect by our own code using `Delphes CMS_PhaseII` cards [87].

Electrons (muons) are selected by requiring that $p_T > 10$ GeV and $|\eta| < 2.47$ (2.5), jets are required to have $p_T > 20$ GeV and $|\eta| < 3$. We adopt the b -tagging formula from the `Delphes` default card where the efficiency is $\varepsilon_b = 0.8 \tanh\left(0.003 p_T^{b\text{-jet}}\right) \times 30 / (1 + 0.086 p_T^{b\text{-jet}})$ (with $p_T^{b\text{-jet}}$ in unit of GeV) [87]. We apply some pre-selection cuts before launching the carefully designed analysis below. First, all events should have exactly two same-sign leptons and the number of jets should be at least 3: $N_{\text{jet}} \geq 3$. Finally we veto any event with b -tagged jet: $N_{b\text{-jet}} = 0$.

3.1.1 Cut-based analysis

The same-sign W pair signal from $H^{\pm\pm} \rightarrow W^{\pm}W^{\pm}$ has been searched for at the LHC by the ATLAS collaboration [52, 53]. In the searches of same-sign dilepton plus jets plus missing energy, the most stringent lower limit on doubly-charged scalar mass is 350 GeV [53]. As a case study, we first consider the scenario of $M_{H^{\pm\pm}} = 400$ GeV, which satisfies the current direct LHC constraints. The kinematic variables we use to distinguish the signal from backgrounds are the missing transverse energy E_T^{miss} , the effective mass M_{eff} defined as scalar sum of transverse momenta of all reconstructed leptons, jets, and missing energy, the separation $\Delta R_{\ell\ell}$ between two leptons, the azimuthal angle $\Delta\phi(\ell\ell, E_T^{\text{miss}})$ between the two lepton system and E_T^{miss} , the invariant mass of all jets M_{jets} , and the cluster transverse mass from jets and E_T^{miss} defined as [88]

$$M_T^{\text{jets}} \equiv \left[\left(\sqrt{M_{\text{jets}}^2 + \left| \sum_j \vec{p}_T^j \right|^2} + E_T^{\text{miss}} \right)^2 - \left| \sum_j \vec{p}_T^j + \vec{E}_T^{\text{miss}} \right|^2 \right]^{1/2}. \quad (3.3)$$

To enhance the signal-to-background ratio, the selection cuts we applied are as follows, and the corresponding cut-flows for the cross sections of signal and backgrounds are collected in Table 3.

- $0.3 < \Delta R_{\ell\ell} < 2.0$. The lower limit of $\Delta R_{\ell\ell}$ separates the leptons for isolation. The leptons in our signal emerge from the decay of two same-sign W bosons which are from the decay of $H^{\pm\pm}$. However, the leptons associated with the background processes emerge from the decays of W and Z bosons which are well separated. Therefore, the leptons in the signal tend to have smaller $\Delta R_{\ell\ell}$. The distributions of $\Delta R_{\ell\ell}$ for the signal and backgrounds are presented in the top left panel of Fig. 5.
- $E_T^{\text{miss}} > 110$ GeV. One of the decay products emerging from $H^{\pm\pm}$ is the light neutral scalar ϕ which decays only into neutrinos and appears to be invisible in the detector. Due to the existence of the massive ϕ along with the neutrinos from W boson decay, our signal tends to have larger missing transverse energy compared to the background processes (see the top right panel of Fig. 5 for distributions). Consequently, we choose a high E_T^{miss} threshold to distinguish the signal from backgrounds.
- $M_{\text{eff}} > 350$ GeV. Borrowed from the SUSY searches [89, 90], the effective mass M_{eff} is a measure of the overall activity of the event. It provides a good discrimination especially for signals with energetic jets. The jets in our signal are from W decay while the jets associated with backgrounds are from the QCD productions, which makes the jets from the signal to be more energetic in general. This can be seen in the middle left panel of Fig. 5. Thus the effective mass associated with the signal is distributed at higher values.
- $M_T^{\text{jets}} > 300$ GeV. Since the decay products from $H^{\pm\pm}$ contain invisible particles, we cannot fully reconstruct its mass. The transverse mass M_T^{jets} is an alternative option in this situation. We choose to reconstruct the transverse mass M_T^{jets} of $H^{\pm\pm}$

Table 3. Cut-flow of the cross sections for signal and SM backgrounds WZ , WW , $t\bar{t}W$, WWW at the HL-LHC with $M_{H^{\pm\pm}} = 400$ GeV.

Cut Selection	Signal [fb]	WZ [fb]	WW [fb]	$t\bar{t}W$ [fb]	WWW [fb]
$0.3 < \Delta R_{\ell\ell} < 2.0$	0.092	4.5	1.3	0.64	0.25
$E_T^{\text{miss}} > 110$ GeV	0.067	1.1	0.41	0.191	0.053
$M_{\text{eff}} > 350$ GeV	0.066	0.95	0.39	0.18	0.039
$M_T^{\text{jets}} > 300$ GeV	0.064	0.94	0.39	0.18	0.038
$150 \text{ GeV} < M_{\text{jets}} < 350 \text{ GeV}$	0.062	0.22	0.067	0.073	0.018
$\Delta\phi(\ell\ell, E_T^{\text{miss}}) < 1.5$	0.049	0.13	0.035	0.040	0.010

using jets and E_T^{miss} in order to reproduce its mass peak as close as possible. From the distributions shown in the middle right panel of Fig. 5, we can see that the transverse mass for the signal peaks around 400 GeV while for backgrounds it peaks at a smaller value. Consequently, a large M_T^{jets} cut can help us to discriminate the signal from backgrounds.

- $150 \text{ GeV} < M_{\text{jets}} < 350 \text{ GeV}$. As mentioned above, the jets in the signal emerge from the hadronic decays of W boson while the jets associated with the main backgrounds are from QCD production. As a result, the invariant mass of all jets from backgrounds has a broader and flatter distribution, while the distribution for the signal is concentrated in the region between the two W boson mass threshold and the doubly-charged scalar mass, as shown in the bottom left panel of Fig. 5. This provides a good observable to distinguish the signal from backgrounds.
- $\Delta\phi(\ell\ell, E_T^{\text{miss}}) < 1.5$. The contributions to E_T^{miss} associated with the signal are neutrinos and the light neutral scalar ϕ from the decay of $H^{\pm\pm}$. The signal decay products include also same-sign dileptons and, consequently, the azimuthal angle between the same-sign dilepton and E_T^{miss} in the signal tends to have a small value. In contrast, the backgrounds do not have such kinematics and thus the distribution of $\Delta\phi(\ell\ell, E_T^{\text{miss}})$ is rather flat for the background processes. The distributions for the signal and backgrounds are shown in the bottom right panel of Fig. 5.

After all the cuts, it is found in Table 3 that the cross section for our signal is only a few times smaller than that for the SM backgrounds. To calculate the signal significance, we use the metric $\sigma = S/\sqrt{S+B}$ where S and B are the numbers of events for signal and backgrounds respectively, and we have not included any systematic uncertainties in our analysis. The expected event yields at the HL-LHC after all the cuts above are shown in Table 4. It is clear that the significance can reach 5σ in the cut-based analysis, which implies a great potential for discovery of the signal $H^{\pm\pm} \rightarrow W^\pm W^\pm \phi$ at the HL-LHC.

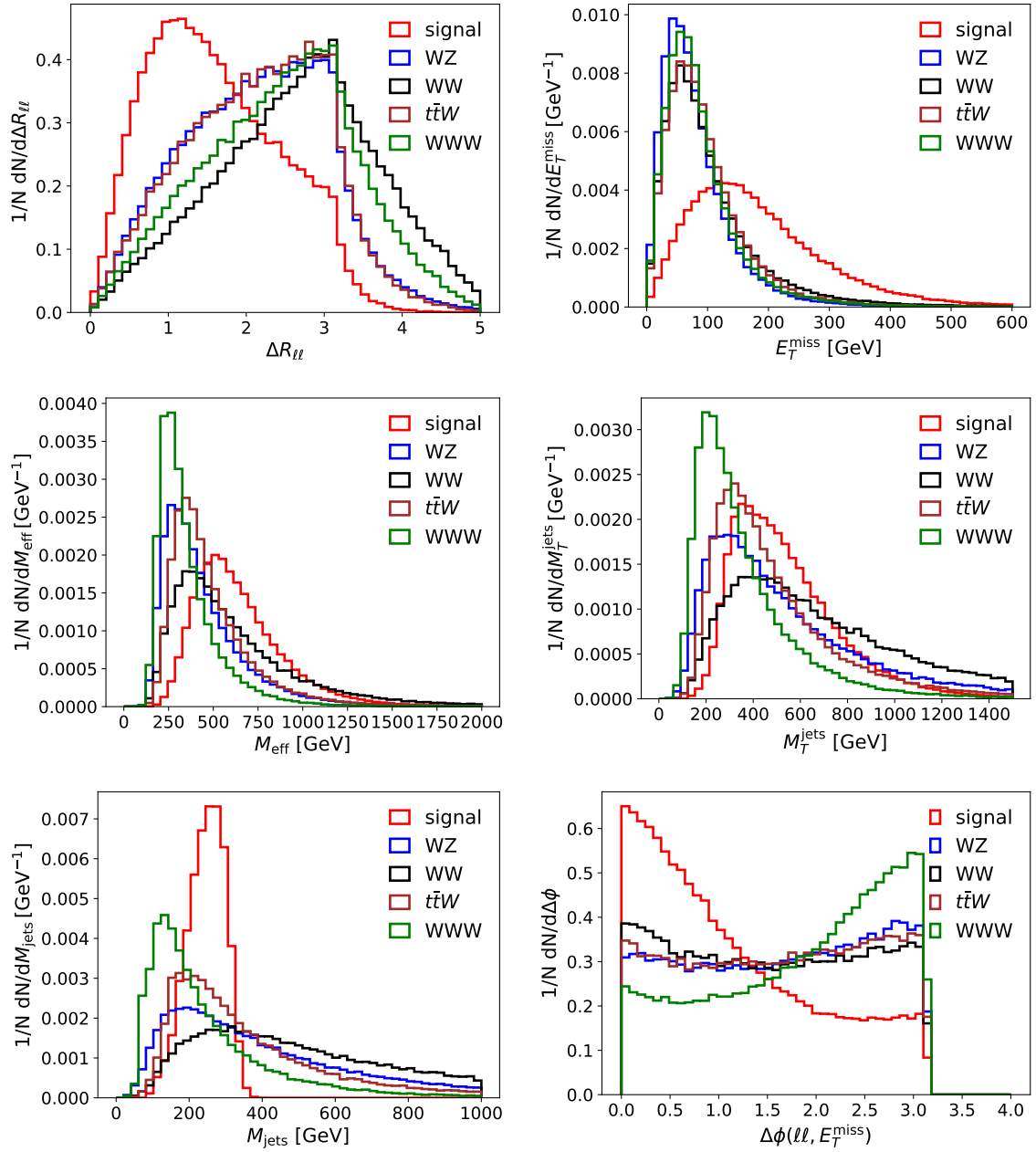


Figure 5. Distributions of observables used in cut-based analysis for the signal $W^\pm W^\pm \phi$ and SM backgrounds WZ , WW , $t\bar{t}W$, WWW : separation of two leptons $\Delta R_{\ell\ell}$ (top left), missing transverse energy E_T^{miss} (top right), effective mass M_{eff} (middle left), transverse mass M_T^{jets} of $H^{\pm\pm}$ defined in Eq. (3.3) (middle right), invariant mass M_{jets} of jets (bottom left), and the azimuthal angle $\Delta\phi(\ell\ell, E_T^{\text{miss}})$ between dilepton and missing energy (bottom right). All the distributions are normalized to be unity.

Table 4. Number of events in cut-based and BDT analysis for signal and backgrounds at the HL-LHC with 3 ab^{-1} luminosity and for $M_{H^{\pm\pm}} = 400 \text{ GeV}$. The last column shows the significance of signal.

	Signal	WZ	WW	$t\bar{t}W$	WWW	Backgrounds	σ
Number of events (cut-based)	145.56	397.54	104.17	120.00	30.42	652.12	5.15
Number of events (BDT-based)	184.56	70.00	23.00	29.30	10.48	132.78	10.36

3.1.2 BDT improvement

In order to further control the backgrounds, we adopt the BDT technique. In particular, we use the XGBoost package [91] to build the BDT. In addition to the variables mentioned above, we also feed the BDT the following variables:

- invariant mass $M_{\ell\ell}$ of same-sign dileptons;
- transverse mass $M_T^{\ell\ell}$ constructed from leptons and E_T^{miss} ;
- azimuthal angles $\Delta\phi(\ell_1, E_T^{\text{miss}})$ and $\Delta\phi(\ell_2, E_T^{\text{miss}})$ between leptons and E_T^{miss} ;
- azimuthal angle $\Delta\phi(j_1, E_T^{\text{miss}})$ between leading jet and E_T^{miss} ;
- separation $\Delta R_{\ell_1 j_1}$ and $\Delta R_{\ell_2 j_1}$ of leptons and leading jet;
- minimum separation $\min\Delta R_{jj}$ of two jets;
- minimum separation $\min\Delta R_{\ell j}$ of leptons and jets;
- minimum invariant mass $\min M_{jj}$ of two jets.

Some of the distributions, such as those for $\min M_{jj}$, $M_{\ell\ell}$, $M_T^{\ell\ell}$ and $\min\Delta R_{jj}$, are shown in Fig. 6. We will see in the lower right panel of Fig. 7 that these distributions are also very important for discriminating the signal from backgrounds.

The hyperparameters we used to train BDT are as follows: the learning rate is 0.1, the number of trees is 500, the maximum depth of each tree is 3, the fraction of events to train tree on is 0.6, the fraction of features to train tree on is 0.8, the minimum sum of instance weight needed in a child is 3, and the minimum loss reduction required to make a further partition on a leaf node of the tree is 0.2.

We split the data set into a training set and a testing set to make sure that there is no over-fitting. The BDT responses for our testing set are shown in the upper panel of Fig. 7. The BDT response close to 1 means the event is more signal-like while the response around 0 means the event is more background-like. We can see that our BDT classifier behaves quite good on the testing set. The receiver operating characteristic curve (ROC curve) of BDT and its feature importance are presented respectively in the lower left and right panels of Fig. 7. The feature importance is measured by “gain”, which is defined as the

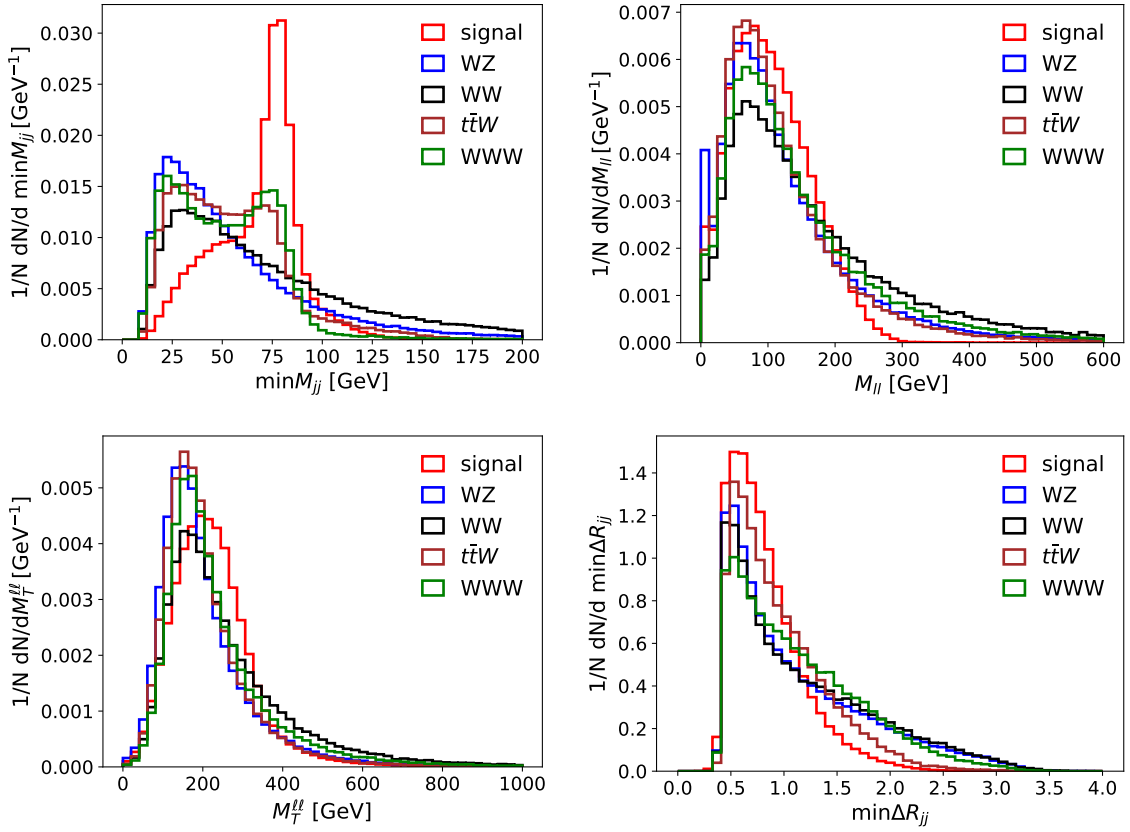


Figure 6. More distributions of variables that are found by BDT to be important for distinguishing signal $W^\pm W^\pm \phi$ from backgrounds WZ , WW , $t\bar{t}W$, WWW : minimum invariant mass $\min M_{jj}$ of two jets (upper left), invariant mass $M_{\ell\ell}$ of same-sign dilepton (upper right), transverse mass $M_T^{\ell\ell}$ of leptons and missing energy (lower left), and minimum separation $\min \Delta R_{jj}$ of two jets (lower right).

average training loss reduction gained when using a feature for splitting. The importance plot shows the top 10 important variables in the BDT training. The observables used in the cut-based analysis rank among the top 10 by the BDT, where the most important one is the effective mass M_{eff} , followed by M_{jets} and E_T^{miss} . In addition, the BDT determines that the distributions $\min M_{jj}$, $M_{\ell\ell}$, $M_T^{\ell\ell}$ and $\min \Delta R_{jj}$ shown in Fig. 6 are also very important.

We choose the BDT cut such that it maximizes the significance of signal. For $M_{H^{\pm\pm}} = 400$ GeV, the event yields of signal and backgrounds after the BDT cut are reported in Table 4. We can see that the BDT can eliminate backgrounds significantly while keeping most of the signal. The significance can reach 10.36 with the help of BDT, which is improved remarkably in comparison to the cut-based method in Section 3.1.1.

3.1.3 Mass reaches

To explore the discovery potential of $H^{\pm\pm}$ in the small Yukawa coupling scenario at the HL-LHC, we generate event samples for the signal process for $M_{H^{\pm\pm}}$ in the range from

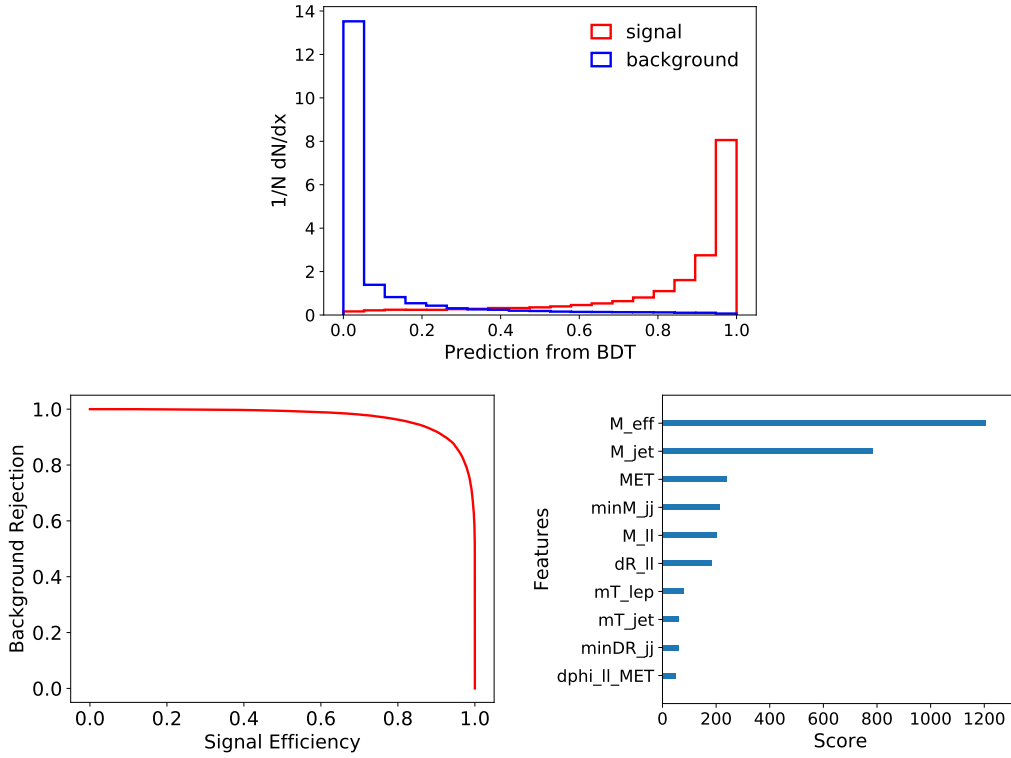


Figure 7. BDT response (upper), ROC curve (lower left) and feature importance (lower right) for the small Yukawa coupling scenario with $M_{H^{\pm\pm}} = 400$ GeV. In the feature importance plot, the variables from top to bottom are respectively M_{eff} , M_{jets} , E_T^{miss} , $\min M_{jj}$, $M_{\ell\ell}$, $\Delta R_{\ell\ell}$, $M_T^{\ell\ell}$, M_T^{jets} , $\min \Delta R_{jj}$ and $\Delta\phi(\ell\ell, E_T^{\text{miss}})$.

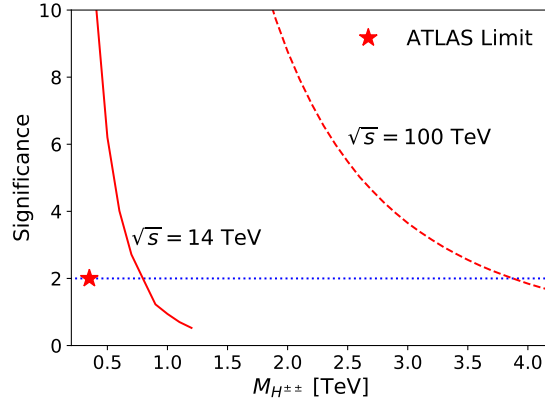


Figure 8. BDT significance as a function of $M_{H^{\pm\pm}}$ at the HL-LHC (solid) and future 100 TeV collider (dashed) for the small Yukawa coupling scenario. The red star is current LHC 2σ limit on $M_{H^{\pm\pm}}$ in the $W^{\pm}W^{\pm}$ channel [53].

300 GeV to 1.2 TeV with the step of 100 GeV. We build BDTs for different masses to discriminate the signal from the SM backgrounds and maximize the significance. The

significance as a function of the doubly-charged scalar mass $M_{H^{\pm\pm}}$ is shown in Figure 8 as the solid line. It is found that we can reach $M_{H^{\pm\pm}} \simeq 800$ GeV at the 2σ significance in the $W^\pm W^\pm \phi$ channel for the small Yukawa scenario at the HL-LHC.

At future 100 TeV hadron colliders such as FCC-hh and SPPC, the production cross section of $H^{\pm\pm}$ can be largely enhanced, as shown in Fig. 4. Following the same BDT analysis as that at 14 TeV LHC, the significance of signal as a function of $M_{H^{\pm\pm}}$ is presented as the dashed line in Figure 8. Benefiting from the large cross section, the prospect of $M_{H^{\pm\pm}}$ can reach up to 3.8 TeV at the 2σ sensitivity at the 100 TeV collider.

3.2 Large Yukawa coupling scenario

Another case of interest in contrast to the previous one is the large Yukawa coupling scenario. According to the low-energy flavor limits in Table 2, most elements of the Yukawa coupling matrix $Y_{\alpha\beta}$ are bounded to be small while $Y_{\mu\mu}$ can be of $\mathcal{O}(1)$ for TeV-scale $H^{\pm\pm}$. Note that the effective coupling between neutrinos and leptonic scalars (H_1 and A_1) in our model is of order $\lambda_{\alpha\beta} \sim 2\sqrt{2}Y_{\alpha\beta} \sin\theta$ (cf. Table 1); therefore, $Y_{\mu\mu} \sim \mathcal{O}(1)$ could also be probed at hadron colliders via the VBF process discussed in our previous study [7]. For example, a $Y_{\mu\mu} = 1.5$ Yukawa coupling leads to an effective coupling $\lambda_{\mu\mu} \sim 0.58$ which is within the 2σ LHC sensitivity in the VBF mode [7]. Although the $Y_{\tau\tau}$ coupling is the least constrained (cf. Table 2), final states involving taus at the hadron colliders are more difficult to analyze; therefore, we only focus on the muon final states and leave the tau signal for a future work.

After considering the constraints from perturbativity and unitarity in Section 2.3, we found that the $Y_{\mu\mu}$ component can be as high as 1.5 as presented in Fig. 3. This is still consistent with the muon $g - 2$ bound given in Table 2 for a TeV-scale $H^{\pm\pm}$. In this scenario, the contributions from other Yukawa coupling elements are negligible, and the doubly-charged scalar $H^{\pm\pm}$ decays predominately into a pair of same-sign muons, *i.e.* $\text{BR}(H^{\pm\pm} \rightarrow \mu^\pm \mu^\pm) \simeq 100\%$. For large $Y_{\mu\mu}$ the main decay channel for the singly-charged scalar will be $H^\pm \rightarrow \mu^\pm \nu$. However, the $H^\pm \rightarrow W^\pm \phi$ channel is still feasible and its BR varies from 10% to 20% depending on the mass of H^\pm , as shown in the lower left panel of Fig. 1. With the W boson decaying hadronically, the ϕ induced signal at the hadron collider emerges from the associated production channel as follows:

$$pp \rightarrow H^{\pm\pm} (\rightarrow \mu^\pm \mu^\pm) H^\mp (\rightarrow W^\mp \phi) \rightarrow \mu^\pm \mu^\pm + 2 \text{jets} + E_T^{\text{miss}},$$

i.e. same-sign muon pair plus two jets from W boson decay plus transverse missing energy from ϕ . We should mention here that the traditional $3\text{-}\mu$ or $4\text{-}\mu$ channels will still be the discovery mode for this scenario, but our choice of the final state and analysis is useful to determine the mass of leptonic scalar ϕ (H_1/A_1) as will be shown in Section 3.2.2.

The same-sign dilepton signals are ‘‘smoking-gun’’ signals of doubly-charged scalars at the high-energy colliders, and have been searched for at the LEP [92–94], Tevatron [95–98], LHC data at 7 TeV [99, 100], 8 TeV [101, 102] and 13 TeV [50, 51]. For the scenario $\text{BR}(H^{\pm\pm} \rightarrow \mu^\pm \mu^\pm) = 100\%$, the current most stringent lower dilepton limit on $M_{H^{\pm\pm}}$ is from the LHC 13 TeV data, being 846 GeV [50]. For illustration purpose, we use

$$M_{H^{\pm\pm}} = 900 \text{ GeV}, \quad M_{H^\pm} = 893 \text{ GeV} \quad (3.4)$$

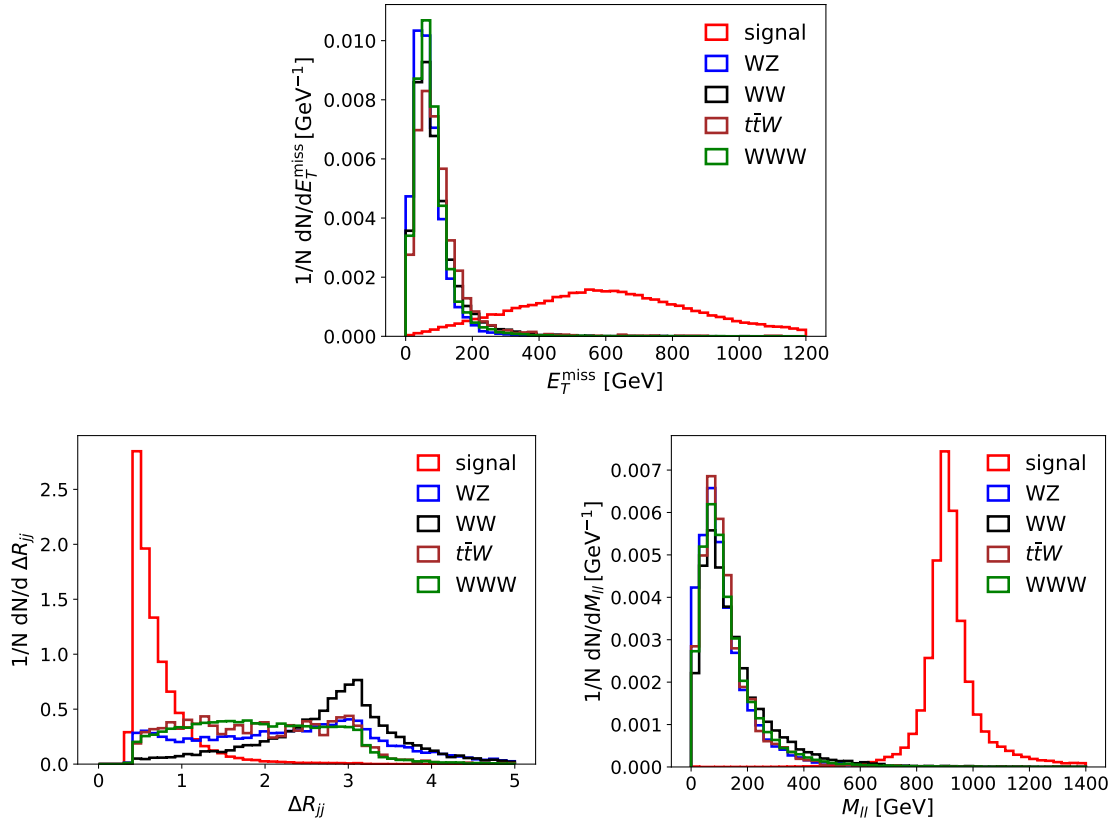


Figure 9. Distributions of E_T^{miss} (upper), ΔR_{jj} (lower left) and $M_{\mu\pm\mu\pm}$ (lower right) in associated production $H^{\pm\pm}H^\mp$ and the SM backgrounds WZ , WW , $t\bar{t}W$, WWW .

as our benchmark scenario for the analysis below.

3.2.1 Analysis and mass reaches

The signal samples are generated by using MadGraph5. Since the final state is similar to the small Yukawa coupling case, we use the same background samples as in Section 3.1. The muon and jet definitions are also kept unchanged. All the events are required to have two reconstructed same-sign muons and two jets without any b -tagged jet. In addition, to further control the backgrounds the following cuts are applied, and the corresponding cut-flows for the cross sections of signal and backgrounds are presented in Table 5.

- $\min\Delta R_{\mu j} > 0.4$ and $\Delta R_{\mu\mu} > 0.3$. This is to satisfy the muon isolation criteria.
- $E_T^{\text{miss}} > 200 \text{ GeV}$. Since E_T^{miss} in the signal is from the scalar $\phi = H_1, A_1$, it tends to have a larger value than the backgrounds with a broader distribution, as shown in the upper panel of Fig. 9.
- $\Delta R_{jj} < 2$. The two jets in the signal are from the decay products of a very energetic W boson, so they tend to be more collimated than the backgrounds. With the

Table 5. Cut-flow of the cross sections for signal and SM backgrounds WZ , WW , $t\bar{t}W$, WWW at the HL-LHC for the large Yukawa coupling scenario (3.4). Backgrounds that are essentially eliminated are denoted by “–”s.

Cut Selection	Signal [fb]	WZ [fb]	WW [fb]	$t\bar{t}W$ [fb]	WWW [fb]
$\min\Delta R_{\mu j} > 0.4$ and $\Delta R_{\mu\mu} > 0.3$	0.0059	1.7	0.81	0.044	0.27
$E_T^{\text{miss}} > 200$ GeV	0.0056	0.036	0.049	0.0027	0.010
$\Delta R_{jj} < 2$	0.0054	0.017	0.013	0.0019	0.0082
$700 \text{ GeV} < M_{\mu^\pm\mu^\pm} < 1100$ GeV	0.050	0.00010	0.00015	–	0.00019

Table 6. Number of events in cut-based and BDT analysis for associated production $H^{\pm\pm}H^\mp$ in the benchmark scenario (3.4) and the SM backgrounds at the HL-LHC with 3 ab^{-1} luminosity. The last column shows the significance of signal. Backgrounds that are essentially eliminated by our cuts are denoted by “–”s.

	Signal	WZ	WW	$t\bar{t}W$	WWW	Backgrounds	σ
Number of events (Cut-based)	14.87	0.32	0.46	–	0.57	1.35	3.69
Number of events (BDT-based)	19.00	–	–	–	0.06	0.06	4.35

distributions shown in the lower left panel of Fig. 9, a small ΔR_{jj} can help us to reduce the backgrounds.

- $700 \text{ GeV} < M_{\mu^\pm\mu^\pm} < 1100$ GeV. Since the same-sign muon pair appears from the decay of the $H^{\pm\pm}$ boson, their Breit–Wigner peak provides a strong discrimination against the SM backgrounds. This can be clearly seen in the lower right panel of Fig. 9.

As a result of very distinct topologies of the signal and backgrounds, the number of background events can be highly suppressed after the cuts, as reported in Table 5. The expected numbers of events at the HL-LHC are shown in Table 6. In the cut-based analysis, the significance can reach $\sigma = 3.67$ for the benchmark scenario in Eq. (3.4).

As in the small Yukawa coupling case in Section 3.1, BDT can help us improve to some extent the sensitivity. In addition to the observables above in cut-and-count analysis, we also use the following observables:

- transverse momenta p_{T,μ_1} and p_{T,μ_2} of the two muons;
- effective mass M_{eff} ;
- invariant mass M_{jj} of two jets;
- total transverse momentum $p_{T,jj}$ of two jets;

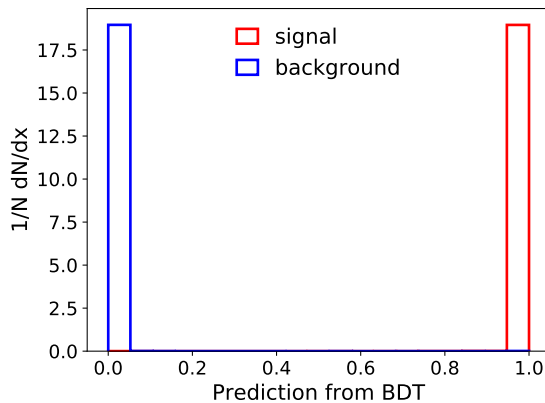


Figure 10. BDT score distribution for the large Yukawa coupling scenario.

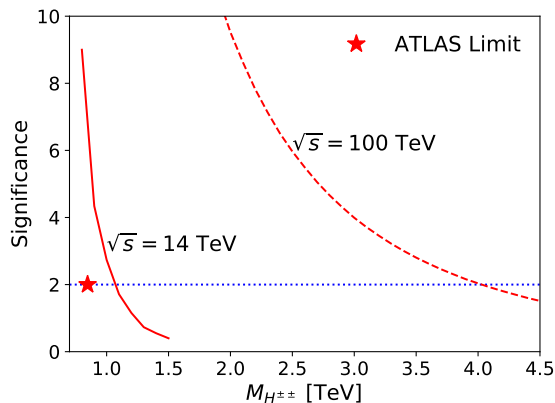


Figure 11. BDT significance as a function of $M_{H^{\pm\pm}}$ at the HL-LHC (solid) and future 100 TeV collider (dashed) for the large Yukawa coupling scenario. The red star indicates the current LHC 2σ limit on $M_{H^{\pm\pm}}$ with 100% BR into $\mu^\pm\mu^\pm$ [50].

- transverse mass M_T constructed from jets and E_T^{miss} ;
- azimuthal angle $\Delta\phi(\mu\mu, E_T^{\text{miss}})$ between two muons and E_T^{miss} .

The BDT score distribution is presented in Fig. 10. As expected, the signal is well separated from the backgrounds. Therefore the BDT can eliminate almost all the background events while keeping most of the signal events. The expected numbers of signal and background events after optimal BDT cuts are collected in the last row of Table 6. With the help of BDT, the sensitivity can reach a higher value at $\sigma = 4.35$.

Since the backgrounds can be highly suppressed by the BDT analysis, the significance will be mainly determined by the cross section of signal, which in turn depends on the mass of $H^{\pm\pm}$. We generate our signal samples in the step of 100 GeV for $M_{H^{\pm\pm}}$ varying from 900 GeV to 1.5 TeV. The resultant significance at the HL-LHC as a function of $M_{H^{\pm\pm}}$ is shown in Fig. 11 as the solid line. It turns out $H^{\pm\pm}$ can be probed up to 1.1 TeV at the 2σ sensitivity at the HL-LHC in the large Yukawa coupling scenario. At a future 100 TeV

collider, the production cross section $\sigma(pp \rightarrow H^{\pm\pm}H^\mp)$ can be enhanced by over one order of magnitude (see Fig. 4). The corresponding prospect of $M_{H^{\pm\pm}}$ can reach up to 4 TeV at the 2σ sensitivity, which is indicated by the dashed line in Fig. 11.

3.2.2 Mass determination of the leptonic scalar ϕ

For the associated production $H^{\pm\pm}H^\mp$ in the large Yukawa coupling case, the only missing particles is $\phi = H_1, A_1$, which provides a possibility to measure its mass. However, at the hadron colliders such as LHC, we can at most determine the transverse momentum of ϕ while its longitudinal momentum is completely lost. Therefore the usual method to determine a particle's mass is not applicable here. An alternative approach is to utilize the transverse mass of a mother particle whose decay products contain a massive invisible daughter particle. To achieve this, we need to modify the definition of transverse mass in Eq. (3.3). In that equation, we do not consider the mass of the missing particles but simply assume the transverse energy of missing particles to be the same as the missing transverse momentum. The modified definition of missing transverse energy is

$$E_T^{\text{miss}}(\tilde{m}) = \sqrt{\tilde{m}^2 + p_{T,\text{miss}}^2}, \quad (3.5)$$

where \tilde{m} is the assumed mass of ϕ , and $p_{T,\text{miss}}$ is the missing transverse momentum. Thus the cluster transverse mass M_T can be re-expressed as a function of the assumed mass \tilde{m} :

$$M_T(\tilde{m}) = \left[\left(\sqrt{M_{\text{jets}}^2 + \left| \sum_j \vec{p}_T^j \right|^2} + \sqrt{\tilde{m}^2 + p_{T,\text{miss}}^2} \right)^2 - \left| \sum_j \vec{p}_T^j + \vec{p}_{T,\text{miss}} \right|^2 \right]^{1/2}. \quad (3.6)$$

As shown in Refs. [103, 104], the endpoint of M_T distribution will increase with the assumed mass \tilde{m} , and a kink will appear at the point of $\tilde{m} = m$ when the assumed mass \tilde{m} is equal to the real mass m of the invisible daughter particle.

As an explicit example, we choose the scalar mass $m_\phi = 89.28$ GeV, and the masses of charged scalars are set as in Eq. (3.4). We calculate the transverse mass M_T of the simulated events by Eq. (3.6) with different choices of \tilde{m} , and then use package `EdgeFinder` [105] to find the endpoint of M_T distribution for each \tilde{m} choice. The result is shown in Fig. 12. By fitting the data points, a kink is found at $\tilde{m} = (93.60 \pm 11.43)$ GeV. Comparing \tilde{m} at the kink with the real mass m_ϕ , we find that this method provides a great potential for measuring the mass of the invisible light scalar $\phi = H_1, A_1$ at the LHC.

We note that the fitting process may be associated with some uncertainties for both M_T edges and m_ϕ . To test the robustness of fitting result, we smear the M_T edge according to the initial error bars from the `EdgeFinder` package in a Normal distribution. Using 100 points for trial, we find that the mass determination by the kink yields a result $\tilde{m} = (93.55 \pm 11.41)$ GeV. Since the uncertainty range does not change, we can state that the kink-finding method leads to a rather reliable mass determination. It should be noted that it is difficult to apply the mass determination technique used here to the small Yukawa coupling scenario in Section 3.1, since in that case ϕ is from $H^{\pm\pm}$ decay, which leads to the

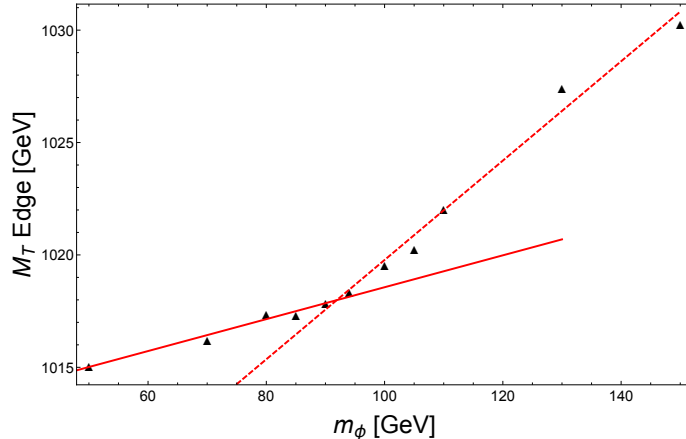


Figure 12. M_T endpoints (black triangles) from EdgeFinder fitting [105] as a function of assumed trial mass m_ϕ . The red straight lines are from linear fittings as an illustration of kink position.

appearance of missing energy from both neutrinos from W boson decay and the invisible scalar ϕ .

4 Discussions and conclusion

In this paper, we have presented a global $(B - L)$ -conserved UV-complete neutrino mass model which contains a scalar triplet Δ and a singlet Φ both carrying a $B - L$ charge of $+2$. From mixing of the neutral components of Δ with Φ , this model features new neutrino interactions along with a pair of (light) leptonic scalars H_1 and A_1 , collectively denoted by ϕ . The light leptonic scalar ϕ induces very rich phenomenological consequences. We list here the main features of the model, allowed parameter space and the prospects of discovering this model at the HL-LHC and a future 100 TeV collider. Here are the main points:

- The proposed model looks similar to the Type-II seesaw model. But unlike the standard Type-II seesaw model, the neutral component of the triplet Δ of this model does not acquire any VEV. As a result, there is no Majorana mass term, neutrinos are Dirac fermions, and the $SU(2)_L$ custodial symmetry remains unbroken in this model.
- In light of all the low-energy LFV constraints, the coupling $Y_{\mu\mu}$ can be as large as $\mathcal{O}(1)$ for a TeV-scale $H^{\pm\pm}$ while all other Yukawa couplings are more stringently constrained (see Fig. 2 and Table 2). Using RGEs, we have also determined the largest values of λ_8 and $Y_{\alpha\beta}$ at the EW scale in order to keep the theory perturbative all the way to the UV-complete scale, as shown in Fig. 3. It is remarkable that as a good approximation the perturbativity limits can be obtained analytically. We checked also the unitarity constraints for these couplings and found them to be much weaker compared to the perturbativity limits.

- Originating from the gauge couplings, $H^{\pm\pm}$ and H^\pm can decay into the light leptonic scalar $\phi = H_1, A_1$ via $H^{\pm\pm} \rightarrow W^\pm W^\pm \phi$ and $H^\pm \rightarrow W^\pm \phi$. The scalar ϕ provides additional sources of missing energy (along with the neutrinos from the decays of W when the leptonic final states are selected) since it decays only into neutrinos, *i.e.* $\phi \rightarrow \nu\nu$. These new decay channels $H^{\pm\pm} \rightarrow W^\pm W^\pm \phi$ and $H^\pm \rightarrow W^\pm \phi$ dominate for small $Y_{\alpha\beta}$. For $\mathcal{O}(1)$ values of $Y_{\alpha\beta}$, $H^{\pm\pm}$ and H^\pm decay primarily into $\ell^\pm \ell^\pm$ and $\ell^\pm \nu$ respectively, while the decay $H^\pm \rightarrow W^\pm \phi$ can still occur with a BR of 10% – 20% level, as shown in the left panels of Fig. 1, which is used for signal selection in this case.
- For our LHC analysis, we utilized the presence of the new source of missing energy from ϕ in the decays of $H^{\pm\pm}$ and H^\pm , and the BDT analysis can improve significantly the signal significance, in particular for the small Yukawa coupling case. At the HL-LHC, we found that for small and large $Y_{\alpha\beta}$, the 2σ (5σ) sensitivity reaches for $H^{\pm\pm}$ are respectively 800 (500) GeV and 1.1 (0.8) TeV (see Tables 4 and 6), as denoted by the solid lines in Figs. 8 and 11. These prospects are well above the current LHC constraints.
- At a future 100 TeV collider, the production cross section of $H^{\pm\pm}$ can be enhanced by over one order of magnitude in both pair production and associated production channels (see Fig. 4). Therefore the mass reaches of $H^{\pm\pm}$ can be largely improved via the observation of ϕ induced signals. For the small and large Yukawa coupling cases, the mass $M_{H^{\pm\pm}}$ can reach up to 3.8 (2.6) TeV and 4 (2.7) TeV respectively at the 2σ (5σ) significance (see Tables 4 and 6), as indicated by the dashed lines in Figs. 8 and 11.
- In the large Yukawa coupling scenario, the missing transverse energy is completely from the invisible light scalar ϕ at the parton level, and the mass m_ϕ can be determined with 10% accuracy at the LHC via the transverse mass distributions associated with jets and missing energy. This is demonstrated in Fig. 12.

In this paper, we have focused on the light leptonic scalar case with mass $M_h/2 < M_\phi \lesssim \mathcal{O}(100 \text{ GeV})$. It should be noted that the analysis in this paper can be generalized to the cases with relatively heavier leptonic scalars ϕ , say with masses of few hundreds of GeV or even larger. Then the ϕ -induced signals will depend largely on the mass M_ϕ . The light ϕ induced signal in this paper can also be compared with the searches of $H^{\pm\pm}$ at future hadron colliders in the standard Type-II seesaw. For instance, the $H^{\pm\pm}$ mass reach has been estimated in the standard Type-II scenario for the LHC and future 100 TeV colliders in Refs. [40, 79]. In a large region of parameter space of Type-II seesaw, the bosonic decay channel $H^{\pm\pm} \rightarrow W^\pm W^\pm$ dominates, and the mass reach of $H^{\pm\pm}$ is found to be 1.8 TeV at 5σ at the 100 TeV collider, which is smaller than our reach of ~ 2.6 TeV in both the large and small Yukawa coupling scenarios (cf. the dashed line in Figs. 8 and 11). The better reach in our model is due to the extra source of missing energy via ϕ . This makes the signal in our model more easily distinguishable from the SM backgrounds.

Table 7. Trilinear scalar couplings.

Vertices	Couplings
$H_1 H_1 h, A_1 A_1 h$	$-i((\lambda_1 + \lambda_4) \sin^2 \theta + \lambda_6 \cos^2 \theta + \lambda_8 \sin 2\theta)v$
$H_2 H_2 h, A_2 A_2 h$	$-i((\lambda_1 + \lambda_4) \cos^2 \theta + \lambda_6 \sin^2 \theta - \lambda_8 \sin 2\theta)v$
$H_1 H_2 h, A_1 A_2 h$	$\frac{1}{2}i((\lambda_1 + \lambda_4 - \lambda_6) \sin 2\theta + 2\lambda_8 \cos 2\theta)v$
$H^+ H^- h$	$-i(\lambda_1 + \frac{1}{2}\lambda_4)v$
$H^{++} H^{--} h$	$-i\lambda_1 v$

Acknowledgments

We thank André de Gouvêa for discussions and collaboration on the previous related publication [7], which motivated this work. The work of PSBD was supported in part by the U.S. Department of Energy under Grant No. DE-SC0017987, by the Neutrino Theory Network Program and by a Fermilab Intensity Frontier Fellowship. The work of BD was supported in part by the U.S. Department of Energy under grant No. DE-SC0010813. TG was partly supported by the U.S. Department of Energy under grant No. DE-FG02-95ER40896, the PITT PACC, and by the FAPESP process no. 2019/17182-0. The work of TH and HQ was supported in part by the U.S. Department of Energy under grant No. DE-FG02-95ER40896 and in part by the PITT PACC. YZ is partially supported by “the Fundamental Research Funds for the Central Universities”. This work was partly performed at the Aspen Center for Physics, which is supported by National Science Foundation grant PHY-1607611.

A Feynman rules

This appendix summarizes all the interaction vertices and their Feynman Rules for the model presented in Section 2. The model contains three CP-even scalars h, H_1, H_2 ; two CP-odd scalars A_1, A_2 ; the singly-charged scalars H^\pm ; and the doubly-charged scalars $H^{\pm\pm}$. The component h from the $SU(2)_L$ -doublet is identified with the 125 GeV SM Higgs boson. In our convention, H_1 is lighter than H_2 , and A_1 is lighter than A_2 . The trilinear and quartic scalar couplings are collected in Tables 7 and 8 respectively, the trilinear and quartic gauge couplings are presented in Tables 9 and 10 respectively, and the Yukawa couplings can be found in Table 11.

B The functions G and \mathcal{F}

For the decays in Eq. (2.17), the function $G(x, y)$ is given by

$$G(x, y) = \frac{1}{12y} \left\{ 2(-1+x)^3 - 9(-1+x^2)y + 6(-1+x)y^2 \right. \\ \left. + 6(1+x-y)y\sqrt{-\lambda(x, y)} \left[\arctan\left(\frac{-1+x-y}{\sqrt{-\lambda(x, y)}}\right) + \arctan\left(\frac{-1+x+y}{\sqrt{-\lambda(x, y)}}\right) \right] \right\}$$

Table 8. Quartic scalar couplings

Vertices	Couplings
hhH_1H_1, hhA_1A_1	$-i(\lambda_6 \cos^2 \theta - \lambda_8 \sin 2\theta + (\lambda_1 + \lambda_4) \sin^2 \theta)$
hhH_2H_2, hhA_2A_2	$-i(\lambda_1 \cos^2 \theta + \lambda_4 \cos^2 \theta + \lambda_8 \sin 2\theta + \lambda_6 \sin^2 \theta)$
hhH_2H_1, hhA_2A_1	$i(\lambda_8 \cos 2\theta - \frac{1}{2}(\lambda_1 + \lambda_4 - \lambda_6) \sin 2\theta)$
$H_1H_1H_1H_1, A_1A_1A_1A_1$	$-6i(\lambda_5 \cos^2 \theta + \lambda_7 \cos^2 \theta \sin^2 \theta + (\lambda_2 + \lambda_3) \sin^4 \theta)$
$H_1H_1A_1A_1$	$-2i(\lambda_5 \cos^4 \theta + \lambda_7 \cos^2 \theta \sin^2 \theta + (\lambda_2 + \lambda_3) \sin^4 \theta)$
$H_2H_2H_2H_2, A_2A_2A_2A_2$	$-6i((\lambda_2 + \lambda_3) \cos^4 \theta + \lambda_7 \cos^2 \theta \sin^2 \theta + \lambda_5 \sin^4 \theta)$
$H_2H_2A_2A_2$	$-2i((\lambda_2 + \lambda_3) \cos^4 \theta + \lambda_7 \cos^2 \theta \sin^2 \theta + \lambda_5 \sin^4 \theta)$
$H_1H_1H_1H_2, A_1A_1A_1A_2$	$\frac{3}{2}i(-\lambda_2 - \lambda_3 + \lambda_5 + (\lambda_2 + \lambda_3 + \lambda_5 - \lambda_7) \cos 2\theta) \sin 2\theta$
$H_1H_1H_2H_2, A_1A_1A_2A_2$	$-\frac{1}{4}i(3(\lambda_2 + \lambda_3 + \lambda_5) + \lambda_7 - 3(\lambda_2 + \lambda_3 + \lambda_5 - \lambda_7) \cos 4\theta)$
$H_1H_2H_2H_2, A_1A_2A_2A_2$	$-\frac{3}{2}i(\lambda_2 + \lambda_3 - \lambda_5 + (\lambda_2 + \lambda_3 + \lambda_5 - \lambda_7) \cos 2\theta) \sin 2\theta$
$H_1H_1A_2A_2, H_2H_2A_1A_1$	$-\frac{1}{4}i(\lambda_2 + \lambda_3 + \lambda_5 + 3\lambda_7 - (\lambda_2 + \lambda_3 + \lambda_5 - \lambda_7) \cos 4\theta)$
$H_1H_2A_2A_2, H_2H_2A_1A_2$	$-\frac{1}{2}i(\lambda_2 + \lambda_3 - \lambda_5 + (\lambda_2 + \lambda_3 + \lambda_5 - \lambda_7) \cos 2\theta) \sin 2\theta$
$H_1H_1A_1A_2, H_1H_2A_1A_1$	$\frac{1}{2}i(-\lambda_2 - \lambda_3 + \lambda_5 + (\lambda_2 + \lambda_3 + \lambda_5 - \lambda_7) \cos 2\theta) \sin 2\theta$
$H_1H_2A_1A_2$	$-\frac{1}{2}i(\lambda_2 + \lambda_3 + \lambda_5 - \lambda_7) \sin^2 2\theta$
H^+H^-hh	$-i(\lambda_1 + \frac{1}{2}\lambda_4)$
$H^+H^-H_1H_1, H^+H^-A_1A_1$	$-i(\lambda_7 \cos^2 \theta + 2(\lambda_2 + \lambda_3) \sin^2 \theta)$
$H^+H^-H_2H_2, H^+H^-A_2A_2$	$-i(2(\lambda_2 + \lambda_3) \cos^2 \theta + \lambda_7 \sin^2 \theta)$
$H^+H^-H_1H_2, H^+H^-A_1A_2$	$-i(\lambda_2 + \lambda_3 - \frac{1}{2}\lambda_7) \sin 2\theta$
$H^+H^+H^-H^-$	$-2i(2\lambda_2 + \lambda_3)$
$H^{++}H^{--}hh$	$-i\lambda_1$
$H^{++}H^{--}H_1H_1, H^{++}H^{--}A_1A_1$	$-i(\lambda_7 \cos^2 \theta + 2\lambda_2 \sin^2 \theta)$
$H^{++}H^{--}H_2H_2, H^{++}H^{--}A_2A_2$	$-i(2\lambda_2 \cos^2 \theta + \lambda_7 \sin^2 \theta)$
$H^{++}H^{--}H_1H_2, H^{++}H^{--}A_1A_2$	$-i(\lambda_2 - \frac{1}{2}\lambda_7) \sin 2\theta$
$H^{++}H^-H^-H_1, H^{++}H^-H^-H_2$	$\sqrt{2}i\lambda_3 \sin \theta$
$H^{++}H^-H^-A_1, H^{++}H^-H^-A_2$	$\sqrt{2}\lambda_3 \sin \theta$
$H^{++}H^{--}H^+H^-$	$-2i(\lambda_2 + \lambda_3)$
$H^{++}H^{++}H^{--}H^{--}$	$-4i(\lambda_2 + \lambda_3)$

$$-3y \left[1 + (x - y)^2 - 2y \right] \log x \left. \vphantom{-3y} \right\}. \quad (\text{B.1})$$

For the decays in Eq. (2.19), the function \mathcal{F} is defined as

$$\begin{aligned}
F &= 4 + \frac{1}{2}(x - 2)^2 \\
&+ \frac{1}{2(y - u)^2} [(y - 1)^2 - 2r(y + 1) + r^2] [(y - 1)^2 - 2w(y + 1) + w^2] \\
&+ \frac{1}{2(z - u)^2} [(z - 1)^2 - 2r(z + 1) + r^2] [(z - 1)^2 - 2w(z + 1) + w^2] \\
&+ \frac{1}{(y - u)(z - u)} [(y - r)(z - w) + (y + z + r + w - 3)]
\end{aligned}$$

Table 9. Trilinear gauge couplings. Here p_1, p_2 are the momenta of the first and second particles in the vertices.

Vertices	Couplings
$A_1 H_1 Z_\mu$	$\frac{g_L}{c_W} (p_1 - p_2)_\mu \sin^2 \theta$
$A_2 H_2 Z_\mu$	$\frac{g_L}{c_W} (p_1 - p_2)_\mu \cos^2 \theta$
$A_1 H_2 Z_\mu, A_2 H_1 Z_\mu$	$-\frac{g_L}{2 c_W} (p_1 - p_2)_\mu \sin 2\theta$
$H^+ H^- \gamma_\mu$	$i e (p_1 - p_2)_\mu$
$H^+ H^- Z_\mu$	$-i e \frac{s_W}{c_W} (p_1 - p_2)_\mu$
$H^+ H_1 W_\mu^-$	$-i \frac{g_L}{\sqrt{2}} (p_1 - p_2)_\mu \sin \theta$
$H^+ H_2 W_\mu^-$	$i \frac{g_L}{\sqrt{2}} (p_1 - p_2)_\mu \cos \theta$
$H^+ A_1 W_\mu^-$	$-\frac{g_L}{\sqrt{2}} (p_1 - p_2)_\mu \sin \theta$
$H^+ A_2 W_\mu^-$	$\frac{g_L}{\sqrt{2}} (p_1 - p_2)_\mu \cos \theta$
$H^{++} H^{--} \gamma_\mu$	$2i e (p_1 - p_2)_\mu$
$H^{++} H^{--} Z_\mu$	$i e \frac{c_W^2 - s_W^2}{c_W s_W} (p_1 - p_2)_\mu$
$H^{++} H^- W_\mu^-$	$-i g_L (p_1 - p_2)_\mu$

$$\begin{aligned}
& \times [(z-r)(y-w) + (y+z+r+w-3)] \\
& - \frac{1}{y-u} [(x-2)(y-r-1)(y-w+1) \\
& + 2(y-r-1)^2 + 2(z-r-1)^2 + 2(x-2)(z-r-1) - 8r] \\
& - \frac{1}{z-u} [(x-2)(z-r-1)(z-w+1) \\
& + 2(y-r-1)^2 + 2(z-r-1)^2 + 2(x-2)(y-r-1) - 8r] , \tag{B.2}
\end{aligned}$$

where we have defined

$$x \equiv \frac{m_{12}^2}{M_W^2}, \quad y \equiv \frac{m_{23}^2}{M_W^2}, \quad z \equiv \frac{m_{13}^2}{M_W^2}, \quad r \equiv \frac{m_\phi^2}{M_W^2}, \quad u \equiv \frac{M_{H^\pm}^2}{M_W^2}, \quad w \equiv \frac{M_{H^{\pm\pm}}^2}{M_W^2}. \tag{B.3}$$

C One-loop RGEs

In this appendix, we list the β -functions for all the one-loop RGEs for the gauge couplings, quartic couplings and Yukawa couplings in our model. These were obtained using the PyR@TE package [106]. For simplicity, we keep only the Yukawa coupling $Y_{\mu\mu}$ in the matrix $Y_{\alpha\beta}$. The gauge coupling g_Y is normalized to be $g_1 = \sqrt{3/5}g_Y$ [107].

$$(4\pi)^2 \beta_{g_S} = -7g_S^3, \tag{C.1}$$

$$(4\pi)^2 \beta_{g_L} = -\frac{3}{2}g_L^3, \tag{C.2}$$

Table 10. Quartic gauge couplings.

Vertices	Couplings
$H_1 H_1 Z_\mu Z_\nu, A_1 A_1 Z_\mu Z_\nu$	$2i \frac{g_L^2}{c_W^2} \sin^2 \theta g_{\mu\nu}$
$H_2 H_2 Z_\mu Z_\nu, A_2 A_2 Z_\mu Z_\nu$	$2i \frac{g_L^2}{c_W^2} \cos^2 \theta g_{\mu\nu}$
$H_1 H_2 Z_\mu Z_\nu, A_1 A_2 Z_\mu Z_\nu$	$-i \frac{g_L^2}{c_W^2} \sin 2\theta g_{\mu\nu}$
$H_1 H_1 W_\mu^+ W_\nu^-, A_1 A_1 W_\mu^- W_\nu^-$	$i g_L^2 \sin^2 \theta g_{\mu\nu}$
$H_2 H_2 W_\mu^+ W_\nu^-, A_2 A_2 W_\mu^+ W_\nu^-$	$i g_L^2 \cos^2 \theta g_{\mu\nu}$
$H_1 H_2 W_\mu^+ W_\nu^-, A_1 A_2 W_\mu^+ W_\nu^-$	$-\frac{1}{2} i g_L^2 \sin 2\theta g_{\mu\nu}$
$H^+ H^- \gamma_\mu \gamma_\nu$	$2i e^2 g_{\mu\nu}$
$H^+ H^- Z_\mu Z_\nu$	$2i e^2 \frac{s_W^2}{c_W^2} g_{\mu\nu}$
$H^+ H^- Z_\mu \gamma_\nu$	$-2i e^2 \frac{s_W}{c_W} g_{\mu\nu}$
$H^+ H^- W_\mu^+ W_\nu^-$	$2i g_L^2 g_{\mu\nu}$
$H^+ H_1 W_\mu^- \gamma_\nu$	$-i \frac{e^2}{\sqrt{2} s_W} \sin \theta g_{\mu\nu}$
$H^+ H_2 W_\mu^- \gamma_\nu$	$i \frac{e^2}{\sqrt{2} s_W} \cos \theta g_{\mu\nu}$
$H^+ A_1 W_\mu^- \gamma_\nu$	$-\frac{e^2}{\sqrt{2} s_W} \sin \theta g_{\mu\nu}$
$H^+ A_2 W_\mu^- \gamma_\nu$	$\frac{e^2}{\sqrt{2} s_W} \cos \theta g_{\mu\nu}$
$H^+ H_1 W_\mu^- Z_\nu$	$i \frac{e^2}{\sqrt{2} c_W} \left(2 + \frac{c_W^2}{s_W^2} \right) \sin \theta g_{\mu\nu}$
$H^+ H_2 W_\mu^- Z_\nu$	$-i \frac{e^2}{\sqrt{2} c_W} \left(2 + \frac{c_W^2}{s_W^2} \right) \cos \theta g_{\mu\nu}$
$H^+ A_1 W_\mu^- Z_\nu$	$\frac{e^2}{\sqrt{2} c_W} \left(2 + \frac{c_W^2}{s_W^2} \right) \sin \theta g_{\mu\nu}$
$H^+ A_2 W_\mu^- Z_\nu$	$-\frac{e^2}{\sqrt{2} c_W} \left(2 + \frac{c_W^2}{s_W^2} \right) \cos \theta g_{\mu\nu}$
$H^{++} H^{--} \gamma_\mu \gamma_\nu$	$8i e^2 g_{\mu\nu}$
$H^{++} H^{--} Z_\mu Z_\nu$	$2i g_L^2 \frac{(c_W^2 - s_W^2)^2}{c_W^2} g_{\mu\nu}$
$H^{++} H^{--} Z_\mu \gamma_\nu$	$4i e^2 \frac{c_W^2 - s_W^2}{c_W s_W} g_{\mu\nu}$
$H^{++} H^- W_\mu^+ W_\nu^-$	$i g_L^2 g_{\mu\nu}$
$H^{++} H_1 W_\mu^- W_\nu^-$	$\sqrt{2} i g_L^2 \sin \theta g_{\mu\nu}$
$H^{++} H_2 W_\mu^- W_\nu^-$	$-\sqrt{2} i g_L^2 \cos \theta g_{\mu\nu}$
$H^{++} A_1 W_\mu^- W_\nu^-$	$\sqrt{2} g_L^2 \sin \theta g_{\mu\nu}$
$H^{++} A_2 W_\mu^- W_\nu^-$	$-\sqrt{2} g_L^2 \cos \theta g_{\mu\nu}$
$H^{++} H^- W_\mu^- \gamma_\nu$	$-3i \frac{e^2}{s_W} g_{\mu\nu}$
$H^{++} H^- W_\mu^- Z_\nu$	$i \frac{e^2}{c_W} \left(2 + \frac{c_W^2}{s_W^2} \right) g_{\mu\nu}$

Table 11. Yukawa couplings.

Vertices	Couplings
$H^{++}l_{\alpha}^{-}l_{\beta}^{-}$	$2i Y_{\alpha\beta} P_L$
$H^{+}l_{\alpha}^{-}v_{\beta}$	$\sqrt{2}i Y_{\alpha\beta} P_L$
$H_2\nu_{\alpha}\nu_{\beta}$	$-\sqrt{2}i Y_{\alpha\beta} P_L \cos \theta$
$H_1\nu_{\alpha}\nu_{\beta}$	$-\sqrt{2}i Y_{\alpha\beta} P_L \sin \theta$
$A_2\nu_{\alpha}\nu_{\beta}$	$\sqrt{2} Y_{\alpha\beta} P_L \cos \theta$
$A_1\nu_{\alpha}\nu_{\beta}$	$\sqrt{2} Y_{\alpha\beta} P_L \sin \theta$

$$(4\pi)^2\beta_{g_1} = + \frac{53}{6}g_1^3, \quad (\text{C.3})$$

$$(4\pi)^2\beta_{\lambda} = -9\lambda g_L^2 - 12y_t^4 + 12\lambda_1\lambda_4 + 5\lambda_4^2 + 4\lambda_6^2 + 6\lambda^2 + \frac{3}{2}g_1^4 \\ + 8\lambda_8^2 + 12\lambda_1^2 + \frac{9}{2}g_L^4 + 12\lambda y_t^2 - 12y_t^4 - 3\lambda g_1^2 + 3g_1^2g_L^2, \quad (\text{C.4})$$

$$(4\pi)^2\beta_{\lambda_1} = +\lambda\lambda_4 + 2\lambda_3\lambda_4 + 2\lambda_6\lambda_7 + 3\lambda_1y_t^2 + \lambda_4^2 - \frac{15}{2}\lambda_1g_1^2 + 4\lambda_1|Y_{\mu\mu}|^2 \\ + 6\lambda_2\lambda_4 + 4\lambda_1^2 + 3\lambda\lambda_1 + 3\lambda_1y_t^2 \\ + 16\lambda_1\lambda_2 + 12\lambda_1\lambda_3 - \frac{33}{2}\lambda_1g_L^2 + 3g_1^4 + 6g_1^2g_L^2 + 6g_L^4, \quad (\text{C.5})$$

$$(4\pi)^2\beta_{\lambda_2} = +2\lambda_1\lambda_4 - 12\lambda_2g_1^2 - 24\lambda_2g_L^2 + \lambda_7^2 + 2\lambda_1^2 + 6\lambda_3^2 - 16|Y_{\mu\mu}|^4 \\ + 24\lambda_2\lambda_3 + 6g_1^4 - 12g_1^2g_L^2 + 15g_L^4 + 28\lambda_2^2 + 8\lambda_2|Y_{\mu\mu}|^2, \quad (\text{C.6})$$

$$(4\pi)^2\beta_{\lambda_3} = -24\lambda_3g_L^2 + \lambda_4^2 - 14|Y_{\mu\mu}|^4 + 24\lambda_2\lambda_3 + 8\lambda_3|Y_{\mu\mu}|^2 + 24g_1^2g_L^2 \\ + 18\lambda_3^2 - 12\lambda_3g_1^2 - 6g_L^4, \quad (\text{C.7})$$

$$(4\pi)^2\beta_{\lambda_4} = +\lambda\lambda_4 + 4\lambda_2\lambda_4 - \frac{15}{2}\lambda_4g_1^2 + 8\lambda_3\lambda_4 + 6\lambda_4y_t^2 - 12g_1^2g_L^2 + 8\lambda_1\lambda_4 + 8\lambda_8^2 \\ + 4\lambda_4^2 - \frac{33}{2}\lambda_4g_L^2 + 4\lambda_4|Y_{\mu\mu}|^2, \quad (\text{C.8})$$

$$(4\pi)^2\beta_{\lambda_5} = +20\lambda_5^2 + 2\lambda_6^2 + 3\lambda_7^2, \quad (\text{C.9})$$

$$(4\pi)^2\beta_{\lambda_6} = +6\lambda_6y_t^2 + 12\lambda_8^2 + 6\lambda_1\lambda_7 + 3\lambda_4\lambda_7 + 4\lambda_6^2 - \frac{3}{2}\lambda_6g_1^2 - \frac{9}{2}\lambda_6g_L^2 \\ + 3\lambda\lambda_6 + 8\lambda_5\lambda_6, \quad (\text{C.10})$$

$$(4\pi)^2\beta_{\lambda_7} = +4\lambda_1\lambda_6 + 16\lambda_2\lambda_7 + 12\lambda_3\lambda_7 - 6\lambda_7g_1^2 + 4\lambda_8^2 \\ + 2\lambda_4\lambda_6 - 12\lambda_7g_L^2 + 4\lambda_7|Y_{\mu\mu}|^2 + 8\lambda_5\lambda_7 + 4\lambda_7^2, \quad (\text{C.11})$$

$$(4\pi)^2\beta_{\lambda_8} = +4\lambda_1\lambda_8 + 6\lambda_4\lambda_8 + 2\lambda_7\lambda_8 + 6\lambda_8y_t^2 + 4\lambda_6\lambda_8 \\ - \frac{9}{2}\lambda_8g_1^2 + 2\lambda_8|Y_{\mu\mu}|^2 - \frac{21}{2}\lambda_8g_L^2 + \lambda\lambda_8, \quad (\text{C.12})$$

$$(4\pi)^2\beta_{y_t} = +\frac{9}{2}y_t^3 - \frac{9}{4}g_L^2y_t - 8g_S^2y_t - \frac{17}{12}g_1^2y_t, \quad (\text{C.13})$$

$$(4\pi)^2\beta_{Y_{\mu\mu}} = -\frac{9}{2}g_L^2Y_{\mu\mu} - \frac{3}{2}g_1^2Y_{\mu\mu} + 8|Y_{\mu\mu}|^2Y_{\mu\mu}. \quad (\text{C.14})$$

D Analytical perturbativity limits

For the gauge couplings g_i , it is trivial to get the analytical one-loop expressions for the couplings, which turn out to be

$$\alpha_i(\mu) = \frac{\alpha_i(v)}{1 - \frac{b_i}{2\pi} \alpha_i(v) \log(\mu/v)}, \quad (\text{D.1})$$

with $\alpha_3 = g_S^2/4\pi$, $\alpha_2 = g_L^2/4\pi$, $\alpha_1 = g_1^2/4\pi$ for the $SU(3)_c$, $SU(2)_L$ and $U(1)_Y$ couplings respectively, and $b_3 = -7$, $b_2 = -3/2$, $b_1 = 53/6$ [cf. Eqs. (C.1)-(C.3)]. For the SM top-quark Yukawa coupling y_t , let us first consider only the y_t^3 and $g_S^2 y_t$ terms on the RHS of Eq. (C.13), *i.e.*:

$$(4\pi)^2 \frac{d}{dt} y_t = \frac{9}{2} y_t^3 - 8g_S^2 y_t. \quad (\text{D.2})$$

To implement the running of g_S , we rewrite the equation above to be in the form of

$$\begin{aligned} 8\pi^2 \left[\frac{1}{y_t^2} \frac{d}{dt} y_t^2 + \frac{8}{b_3} \frac{1}{\alpha_3} \frac{d}{dt} \alpha_3 \right] &= \frac{9}{2} y_t^3, \\ \text{or, } 8\pi^2 \frac{d}{dt} \log \left(y_t^2 \alpha_3^{8/b_3} \right) &= \frac{9}{2} y_t^2. \end{aligned} \quad (\text{D.3})$$

Then we can obtain the analytical running of y_t :

$$y_t^2(\mu) \simeq y_t^2(v) \left(\frac{\alpha_3(v)}{\alpha_3(\mu)} \right)^{8/b_3} \left[1 - \frac{9}{16\pi^2} y_t^2(v) \alpha_3^{8/b_3}(v) \int_0^t dt' \alpha_3^{-8/b_3}(t') \right]^{-1}. \quad (\text{D.4})$$

If we include also the $g_L^2 y_t$ and $g_1^2 y_t$ terms in Eq. (C.13), it is straightforward to get the full analytical one-loop solution for y_t :

$$y_t^2(\mu) = y_t^2(v) \left(\frac{E_\alpha(v)}{E_\alpha(\mu)} \right) \left[1 - \frac{9}{16\pi^2} y_t^2(v) E_\alpha(v) \int_0^t dt' E_\alpha^{-1}(t') \right]^{-1}, \quad (\text{D.5})$$

where the function

$$E_\alpha(\mu) = \alpha_3^{8/b_3}(\mu) \alpha_2^{9/4b_2}(\mu) \alpha_1^{17/12b_1}(\mu). \quad (\text{D.6})$$

In the one-loop RGE of $Y_{\mu\mu}$ in Eq. (C.14), if we consider only the $Y_{\mu\mu}^3$ term on the RHS, it is trivial to obtain

$$\alpha_\mu(\mu) = \frac{\alpha_\mu(v)}{1 - \frac{4}{\pi} \alpha_\mu(v) t}, \quad (\text{D.7})$$

where $\alpha_\mu \equiv Y_{\mu\mu}^2/4\pi$. It is clear that the coupling $Y_{\mu\mu}$ will blow up when the t parameter approaches the value of

$$t_c = \log \left(\frac{\mu_c}{v} \right) = \frac{\pi^2}{Y_{\mu\mu}^2(v)}. \quad (\text{D.8})$$

With an initial value of $f(v) = 1.5$, we can get the critical value of $t_c \simeq 4.39$. As in Eq. (D.2), we can first include the gauge coupling g_L , then

$$Y_{\mu\mu}^2(\mu) \simeq Y_{\mu\mu}^2(v) \left(\frac{\alpha_2(v)}{\alpha_2(\mu)} \right)^{9/2b_2} \left[1 - \frac{1}{\pi^2} Y_{\mu\mu}^2(v) \alpha_2^{9/2b_2}(v) \int_0^t dt' \alpha_2^{-9/2b_2}(t') \right]^{-1}. \quad (\text{D.9})$$

In this case, the coupling g_L becomes divergent when the parameter $t_c = 4.64$. If we have all the terms on the RHS of Eq. (C.14), it turns out that

$$Y_{\mu\mu}^2(\mu) = Y_{\mu\mu}^2(v) \left(\frac{\alpha_2(v)}{\alpha_2(\mu)} \right)^{9/2b_2} \left(\frac{\alpha_1(v)}{\alpha_1(\mu)} \right)^{3/2b_1} \times \left[1 - \frac{1}{\pi^2} Y_{\mu\mu}^2(v) \alpha_2^{9/2b_2}(v) \alpha_1^{3/2b_1}(v) \int_0^t dt' \alpha_2^{-9/2b_2}(t') \alpha_1^{-3/2b_1}(t') \right]^{-1}. \quad (\text{D.10})$$

In this case, the critical value $t_c = 4.66$.

We also show the analytical solution of $\lambda_8(\mu)$ below:

$$\lambda_8(\mu) = \lambda_8(v) \exp \left\{ \frac{1}{4\pi^2} \int_v^\mu E_8(\mu) d\mu \right\}, \quad (\text{D.11})$$

where

$$E_8(\mu) = 3y_t(v)^2 \left(1 - \frac{\mu b_3 \alpha_3(v)}{2\pi} \right)^{8/b_3} - \alpha_\mu(v) \left(1 - \frac{4\mu \alpha_\mu(v)}{\pi} \right)^{-1} - \frac{21}{2} \alpha_2(v) \left(1 - \frac{\mu b_2 \alpha_2(v)}{2\pi} \right)^{-1} - \frac{9}{2} \alpha_1(v) \left(1 + \frac{\mu b_1 \alpha_1(v)}{2\pi} \right)^{-1}. \quad (\text{D.12})$$

These results agree well with the full numerical results shown in Fig. 3.

E Unitarity limits

Following the analysis for the Type-II seesaw model [108], the unitarity bounds in our model can be found by diagonalizing the sub-matrices \mathcal{M}_i which correspond to the coefficients for $2 \leftrightarrow 2$ scalar scattering processes. Writing the scalar multiplets explicitly as

$$H = \begin{pmatrix} h^\pm \\ \frac{1}{\sqrt{2}}(h + iZ_1) \end{pmatrix}, \quad \Delta = \begin{pmatrix} \frac{1}{\sqrt{2}}\delta^+ & \delta^{++} \\ \frac{1}{\sqrt{2}}(\xi + iZ_2) & -\frac{1}{\sqrt{2}}\delta^+ \end{pmatrix}, \quad \Phi = \frac{1}{\sqrt{2}}(s + iZ_3), \quad (\text{E.1})$$

the sub-matrices for the initial and final states ($h\xi$, hs , Z_1Z_2 , Z_1Z_3 , hZ_2 , hZ_3 , ξZ_1 , sZ_1 , $h^+\delta^-$, δ^+h^-) and (ξs , Z_2Z_3 , ξZ_3 , sZ_3) respectively are

$$\mathcal{M}_1 = \begin{pmatrix} \lambda_{14} & -\lambda_8 & 0 & \lambda_8 & 0 & 0 & 0 & 0 & \frac{\lambda_4}{2\sqrt{2}} & \frac{\lambda_4}{2\sqrt{2}} \\ -\lambda_8 & \lambda_6 & -\lambda_8 & 0 & 0 & 0 & 0 & 0 & -\frac{\lambda_8}{\sqrt{2}} & -\frac{\lambda_8}{\sqrt{2}} \\ 0 & -\lambda_8 & \lambda_{14} & \lambda_8 & 0 & 0 & 0 & 0 & \frac{\lambda_4}{2\sqrt{2}} & \frac{\lambda_4}{2\sqrt{2}} \\ \lambda_8 & 0 & \lambda_8 & \lambda_6 & 0 & 0 & 0 & 0 & \frac{\lambda_8}{\sqrt{2}} & \frac{\lambda_8}{\sqrt{2}} \\ 0 & 0 & 0 & 0 & \lambda_{14} & -\lambda_8 & 0 & -\lambda_8 & -\frac{i\lambda_4}{2\sqrt{2}} & -\frac{i\lambda_4}{2\sqrt{2}} \\ 0 & 0 & 0 & 0 & -\lambda_8 & \lambda_6 & \lambda_8 & 0 & \frac{i\lambda_8}{\sqrt{2}} & \frac{i\lambda_8}{\sqrt{2}} \\ 0 & 0 & 0 & 0 & 0 & \lambda_8 & \lambda_{14} & \lambda_8 & \frac{i\lambda_4}{2\sqrt{2}} & \frac{i\lambda_4}{2\sqrt{2}} \\ 0 & 0 & 0 & 0 & -\lambda_8 & 0 & \lambda_8 & \lambda_6 & \frac{i\lambda_8}{\sqrt{2}} & -\frac{i\lambda_8}{\sqrt{2}} \\ \frac{\lambda_4}{2\sqrt{2}} & -\frac{\lambda_8}{\sqrt{2}} & \frac{\lambda_4}{2\sqrt{2}} & \frac{\lambda_8}{\sqrt{2}} & \frac{i\lambda_4}{2\sqrt{2}} & -\frac{i\lambda_8}{\sqrt{2}} & -\frac{i\lambda_4}{2\sqrt{2}} & -\frac{i\lambda_8}{\sqrt{2}} & \lambda'_{14} & 0 \\ \frac{\lambda_4}{2\sqrt{2}} & -\frac{\lambda_8}{\sqrt{2}} & \frac{\lambda_4}{2\sqrt{2}} & \frac{\lambda_8}{\sqrt{2}} & -\frac{i\lambda_4}{2\sqrt{2}} & \frac{i\lambda_8}{\sqrt{2}} & \frac{i\lambda_4}{2\sqrt{2}} & \frac{i\lambda_8}{\sqrt{2}} & 0 & \lambda'_{14} \end{pmatrix}, \quad (\text{E.2})$$

$$\mathcal{M}_2 = \begin{pmatrix} \lambda_7 & 0 & 0 & 0 \\ 0 & \lambda_7 & 0 & 0 \\ 0 & 0 & \lambda_7 & 0 \\ 0 & 0 & 0 & \lambda_7 \end{pmatrix}, \quad (\text{E.3})$$

where we have defined the combinations of quartic couplings:

$$\lambda_{ij} \equiv \lambda_i + \lambda_j, \quad \lambda'_{ij} \equiv \lambda_i + \frac{1}{2}\lambda_j. \quad (\text{E.4})$$

The eigenvalues are

$$\lambda_{1,6,7}, \quad \lambda_1 + \lambda_4, \quad \lambda_{146}^\pm, \quad (\text{E.5})$$

with

$$\lambda_{146}^\pm \equiv \frac{1}{4} \left[(2\lambda_1 + 3\lambda_4 + 2\lambda_6) \pm \sqrt{(2\lambda_1 + 3\lambda_4 - 2\lambda_6)^2 + 96\lambda_8^2} \right]. \quad (\text{E.6})$$

For the states ($\frac{1}{\sqrt{2}}hh$, $\frac{1}{\sqrt{2}}\xi\xi$, $\frac{1}{\sqrt{2}}ss$, $\frac{1}{\sqrt{2}}Z_1Z_1$, $\frac{1}{\sqrt{2}}Z_2Z_2$, $\frac{1}{\sqrt{2}}Z_3Z_3$, h^+h^- , $\delta^+\delta^-$, $\delta^{++}\delta^{--}$) with factor of $1/\sqrt{2}$ accounting for the identical particles, the sub-matrix is

$$\mathcal{M}_3 = \begin{pmatrix} \frac{3\lambda}{4} & \frac{\lambda_{14}}{2} & \frac{\lambda_6}{2} & \frac{\lambda}{4} & \frac{\lambda_{14}}{2} & \frac{\lambda_6}{2} & \frac{\lambda}{2\sqrt{2}} & \frac{\lambda'_{14}}{\sqrt{2}} & \frac{\lambda_1}{\sqrt{2}} \\ \frac{\lambda_{14}}{2} & 3\lambda_{23} & \frac{\lambda_7}{2} & \frac{\lambda_{14}}{2} & \lambda_{23} & \frac{\lambda_7}{2} & \frac{\lambda_1}{\sqrt{2}} & \sqrt{2}\lambda_{23} & \sqrt{2}\lambda_2 \\ \frac{\lambda_6}{2} & \frac{\lambda_7}{2} & 3\lambda_5 & \frac{\lambda_6}{2} & \frac{\lambda_7}{2} & \lambda_5 & \frac{\lambda_6}{\sqrt{2}} & \frac{\lambda_7}{\sqrt{2}} & \frac{\lambda_7}{\sqrt{2}} \\ \frac{\lambda}{4} & \frac{\lambda_{14}}{2} & \frac{\lambda_6}{2} & \frac{3\lambda}{4} & \frac{\lambda_{14}}{2} & \frac{\lambda_6}{2} & \frac{\lambda}{2\sqrt{2}} & \frac{\lambda'_{14}}{\sqrt{2}} & \frac{\lambda_1}{\sqrt{2}} \\ \frac{\lambda_{14}}{2} & \lambda_{23} & \frac{\lambda_7}{2} & \frac{\lambda_{14}}{2} & 3\lambda_{23} & \frac{\lambda_7}{2} & \frac{\lambda_1}{\sqrt{2}} & \sqrt{2}\lambda_{23} & \sqrt{2}\lambda_2 \\ \frac{\lambda_6}{2} & \frac{\lambda_7}{2} & \lambda_5 & \frac{\lambda_6}{2} & \frac{\lambda_7}{2} & 3\lambda_5 & \frac{\lambda_6}{\sqrt{2}} & \frac{\lambda_7}{\sqrt{2}} & \frac{\lambda_7}{\sqrt{2}} \\ \frac{\lambda}{2\sqrt{2}} & \frac{\lambda_1}{\sqrt{2}} & \frac{\lambda_6}{\sqrt{2}} & \frac{\lambda}{2\sqrt{2}} & \frac{\lambda_1}{\sqrt{2}} & \frac{\lambda_6}{\sqrt{2}} & \lambda & \lambda'_{14} & \lambda_{14} \\ \frac{\lambda_{14}}{\sqrt{2}} & \sqrt{2}\lambda_{23} & \frac{\lambda_7}{\sqrt{2}} & \frac{\lambda_{14}}{\sqrt{2}} & \sqrt{2}\lambda_{23} & \frac{\lambda_7}{\sqrt{2}} & \lambda'_{14} & 4\lambda'_{23} & 2\lambda_{23} \\ \frac{\lambda_1}{\sqrt{2}} & \sqrt{2}\lambda_2 & \frac{\lambda_7}{\sqrt{2}} & \frac{\lambda_1}{\sqrt{2}} & \sqrt{2}\lambda_2 & \frac{\lambda_7}{\sqrt{2}} & \lambda_{14} & 2\lambda_{23} & 4\lambda_{23} \end{pmatrix}, \quad (\text{E.7})$$

and the eigenvalues are

$$\frac{1}{2}\lambda, \quad 2\lambda_{2,5}, \quad 2(\lambda_2 + \lambda_3), \quad \lambda_{023}, \quad x_{1,2,3}, \quad (\text{E.8})$$

with

$$\lambda_{023} \equiv \frac{1}{4} \left[(\lambda + 4\lambda_2 + 8\lambda_3) \pm \sqrt{(\lambda - 4\lambda_2 - 8\lambda_3)^2 + 16\lambda_4^2} \right] \quad (\text{E.9})$$

and $x_{1,2,3}$ are the roots of the equation

$$\begin{aligned} & x^3 - 2x^2 (3\lambda + 16\lambda_2 + 12\lambda_3 + 8\lambda_5) \\ & + 8x \left[6\lambda(4\lambda_2 + 3\lambda_3 + 2\lambda_5) - 3(2\lambda_1 + \lambda_4)^2 + 64\lambda_2\lambda_5 + 48\lambda_3\lambda_5 - 4\lambda_6^2 - 6\lambda_7^2 \right] \\ & + 32 \left[9\lambda\lambda_7^2 + 12\lambda_5(-2\lambda(4\lambda_2 + 3\lambda_3) + (2\lambda_1 + \lambda_4)^2) + 8\lambda_6^2(4\lambda_2 + 3\lambda_3) - 12\lambda_6\lambda_7(2\lambda_1 + \lambda_4) \right] = 0. \end{aligned} \quad (\text{E.10})$$

The sub-matrix for the states $(hZ_1, \xi Z_2, sZ_3)$ is

$$\mathcal{M}_4 = \begin{pmatrix} \frac{1}{2}\lambda & 0 & 0 \\ 0 & 2(\lambda_2 + \lambda_3) & 0 \\ 0 & 0 & 2\lambda_5 \end{pmatrix}, \quad (\text{E.11})$$

whose eigenvalues are

$$\frac{1}{2}\lambda, \quad 2(\lambda_2 + \lambda_3), \quad 2\lambda_5. \quad (\text{E.12})$$

The sub-matrix for $(hh^+, \xi h^+, sh^+, Z_1 h^+, Z_2 h^+, Z_3 h^+, h\delta^+, \xi\delta^+, s\delta^+, Z_1\delta^+, Z_2\delta^+, Z_3\delta^+, \delta^{++}h^-, \delta^{++}\delta^-)$ is

$$\mathcal{M}_5 = \begin{pmatrix} \frac{\lambda}{2} & 0 & 0 & 0 & 0 & 0 & 0 & \frac{\lambda_4}{2\sqrt{2}} & -\frac{\lambda_8}{\sqrt{2}} & 0 & \frac{i\lambda_4}{2\sqrt{2}} & -\frac{i\lambda_8}{\sqrt{2}} & 0 & -\frac{\lambda_4}{2} \\ 0 & \lambda_1 & 0 & 0 & 0 & 0 & 0 & 0 & 0 & 0 & 0 & 0 & -\frac{\lambda_8}{\sqrt{2}} & -\frac{\lambda_8}{\sqrt{2}} \\ 0 & 0 & \lambda_6 & 0 & 0 & 0 & -\frac{\lambda_8}{\sqrt{2}} & 0 & 0 & -\frac{i\lambda_8}{\sqrt{2}} & 0 & 0 & \sqrt{2}\lambda_8 & 0 \\ 0 & 0 & 0 & \frac{\lambda}{2} & 0 & 0 & 0 & -\frac{i\lambda_4}{2\sqrt{2}} & -\frac{i\lambda_8}{\sqrt{2}} & 0 & \frac{\lambda_4}{2\sqrt{2}} & \frac{\lambda_8}{\sqrt{2}} & 0 & \frac{i\lambda_4}{2} \\ 0 & 0 & 0 & 0 & \lambda_1 & 0 & \frac{i\lambda_4}{2\sqrt{2}} & 0 & 0 & \frac{\lambda_4}{2\sqrt{2}} & 0 & 0 & 0 & 0 \\ 0 & 0 & 0 & 0 & 0 & \lambda_6 & -\frac{i\lambda_8}{\sqrt{2}} & 0 & 0 & \frac{\lambda_8}{\sqrt{2}} & 0 & 0 & \sqrt{2}i\lambda_8 & 0 \\ 0 & \frac{\lambda_4}{2\sqrt{2}} & -\frac{\lambda_8}{\sqrt{2}} & 0 & -\frac{i\lambda_4}{2\sqrt{2}} & \frac{i\lambda_8}{\sqrt{2}} & \lambda'_{14} & 0 & 0 & 0 & 0 & 0 & -\frac{\lambda_4}{2} & 0 \\ \frac{\lambda_4}{2\sqrt{2}} & 0 & 0 & \frac{i\lambda_4}{2\sqrt{2}} & 0 & 0 & 0 & 2\lambda_{23} & 0 & 0 & 0 & 0 & 0 & -\sqrt{2}\lambda_3 \\ -\frac{\lambda_8}{\sqrt{2}} & 0 & 0 & \frac{i\lambda_8}{\sqrt{2}} & 0 & 0 & 0 & 0 & \lambda_7 & 0 & 0 & 0 & 0 & 0 \\ 0 & \frac{i\lambda_4}{2\sqrt{2}} & \frac{i\lambda_8}{\sqrt{2}} & 0 & \frac{\lambda_4}{2\sqrt{2}} & \frac{\lambda_8}{\sqrt{2}} & 0 & 0 & 0 & \lambda'_{14} & 0 & 0 & \frac{i\lambda_4}{2} & 0 \\ -\frac{i\lambda_4}{2\sqrt{2}} & 0 & 0 & \frac{\lambda_4}{2\sqrt{2}} & 0 & 0 & 0 & 0 & 0 & 0 & 2\lambda_{23} & 0 & 0 & \sqrt{2}i\lambda_3 \\ \frac{i\lambda_8}{\sqrt{2}} & 0 & 0 & \frac{\lambda_8}{\sqrt{2}} & 0 & 0 & 0 & 0 & 0 & 0 & 0 & \lambda_7 & 0 & 0 \\ 0 & 0 & \sqrt{2}\lambda_8 & 0 & 0 & -\sqrt{2}i\lambda_8 & -\frac{\lambda_4}{2} & 0 & 0 & -\frac{i\lambda_4}{2} & 0 & 0 & \lambda_{14} & 0 \\ -\frac{\lambda_4}{2} & 0 & 0 & -\frac{i\lambda_4}{2} & 0 & 0 & 0 & -\sqrt{2}\lambda_3 & 0 & 0 & -\sqrt{2}i\lambda_3 & 0 & 0 & 2\lambda_{23} \end{pmatrix}, \quad (\text{E.13})$$

and the eigenvalues are

$$\lambda_1, \quad 2\lambda_{2,5,6,7}, \quad \lambda_1 + \lambda_4, \quad \lambda_1 - \frac{1}{2}\lambda_4, \quad 2(\lambda_2 + \lambda_3), \quad \lambda_{023}^\pm, \quad \lambda_{078}^\pm, \quad \lambda_{146}^\pm, \quad (\text{E.14})$$

with

$$\lambda_{078}^{\pm} \equiv \frac{1}{4} \left[(\lambda + 2\lambda_7) \pm \sqrt{(\lambda - 2\lambda_7)^2 + 32\lambda_8^2} \right]. \quad (\text{E.15})$$

Finally, the sub-matrix for $(\frac{1}{\sqrt{2}}h^+h^+, \frac{1}{\sqrt{2}}\delta^+\delta^+, h^+\delta^+, \delta^{++}h, \delta^{++}\xi, \delta^{++}s, \delta^{++}Z_1, \delta^{++}Z_2, \delta^{++}Z_3)$ is

$$\mathcal{M}_6 = \begin{pmatrix} \frac{\lambda}{2} & 0 & 0 & 0 & 0 & \lambda_8 & 0 & 0 & i\lambda_8 \\ 0 & 2\lambda'_{23} & 0 & 0 & 0 & 0 & 0 & 0 & 0 \\ 0 & 0 & \lambda'_{14} & -\frac{\lambda_4}{2} & 0 & 0 & \frac{i\lambda_4}{2} & 0 & 0 \\ 0 & 0 & -\frac{\lambda_4}{2} & \lambda_1 & 0 & 0 & 0 & 0 & 0 \\ 0 & 0 & 0 & 0 & 2\lambda_2 & 0 & 0 & 0 & 0 \\ \lambda_8 & 0 & 0 & 0 & 0 & \lambda_7 & 0 & 0 & 0 \\ 0 & 0 & -\frac{i\lambda_4}{2} & 0 & 0 & 0 & \lambda_1 & 0 & 0 \\ 0 & 0 & 0 & 0 & 0 & 0 & 0 & 2\lambda_2 & 0 \\ -i\lambda_8 & 0 & 0 & 0 & 0 & 0 & 0 & 0 & \lambda_7 \end{pmatrix}, \quad (\text{E.16})$$

and the eigenvalues are

$$\lambda_{1,7}, \quad 2\lambda_2, \quad 2\lambda_2 + \lambda_3, \quad \lambda_1 + \lambda_4, \quad \lambda_1 - \frac{1}{2}\lambda_4, \quad \lambda_{078}^{\pm}. \quad (\text{E.17})$$

To implement the unitarity bounds, we can set all the eigenvalues in Eqs. (E.5), (E.8), (E.12), (E.14) and (E.17) to be smaller than 8π . As a comparison to the perturbativity bounds, we set the quartic couplings to be the benchmark values,

$$\lambda_1 = 0.1, \quad \lambda_4 = -1, \quad \lambda_{2,3,5,6,7} = 0, \quad (\text{E.18})$$

and check the unitarity bounds on λ_8 . It turns out for this specific benchmark scenario, only the following bounds are relevant to λ_8 :

$$|\lambda_{146}^{\pm}| \leq 8\pi, \quad |\lambda_{078}^{\pm}| \leq 8\pi. \quad (\text{E.19})$$

Among the four constraints, the most stringent one is from λ_{146}^- , which leads to

$$\lambda_8 < 10.0, \quad (\text{E.20})$$

which is much weaker than the perturbativity bound discussed in Section 2.3.

References

- [1] **Particle Data Group Collaboration**, P. A. Zyla *et al.*, *Review of Particle Physics*, PTEP **2020** (2020), no. 8 083C01.
- [2] S. M. Bilenky, *Neutrinos: Majorana or Dirac?*, Universe **6** (2020), no. 9 134.
- [3] P. S. B. Dev *et al.*, *Neutrino Non-Standard Interactions: A Status Report*, SciPost Phys. Proc. **2** (2019) 001, [[1907.00991](https://arxiv.org/abs/1907.00991)].

- [4] M. Lattanzi, R. A. Lineros, and M. Taoso, *Connecting neutrino physics with dark matter*, New J. Phys. **16** (2014), no. 12 125012, [[1406.0004](#)].
- [5] C. Hagedorn, R. N. Mohapatra, E. Molinaro, C. C. Nishi, and S. T. Petcov, *CP Violation in the Lepton Sector and Implications for Leptogenesis*, Int. J. Mod. Phys. A **33** (2018), no. 05n06 1842006, [[1711.02866](#)].
- [6] J. M. Berryman, A. de Gouvêa, K. J. Kelly, and Y. Zhang, *Lepton-Number-Charged Scalars and Neutrino Beamstrahlung*, Phys. Rev. D **97** (2018), no. 7 075030, [[1802.00009](#)].
- [7] A. de Gouvêa, P. S. B. Dev, B. Dutta, T. Ghosh, T. Han, and Y. Zhang, *Leptonic Scalars at the LHC*, JHEP **07** (2020) 142, [[1910.01132](#)].
- [8] C. D. Kreisch, F.-Y. Cyr-Racine, and O. Doré, *Neutrino puzzle: Anomalies, interactions, and cosmological tensions*, Phys. Rev. D **101** (2020), no. 12 123505, [[1902.00534](#)].
- [9] N. Blinov, K. J. Kelly, G. Z. Krnjaic, and S. D. McDermott, *Constraining the Self-Interacting Neutrino Interpretation of the Hubble Tension*, Phys. Rev. Lett. **123** (2019), no. 19 191102, [[1905.02727](#)].
- [10] K.-F. Lyu, E. Stamou, and L.-T. Wang, *Self-interacting neutrinos: Solution to Hubble tension versus experimental constraints*, Phys. Rev. D **103** (2021), no. 1 015004, [[2004.10868](#)].
- [11] A. Das and S. Ghosh, *Flavor-specific interaction favors strong neutrino self-coupling in the early universe*, JCAP **07** (2021) 038, [[2011.12315](#)].
- [12] **FCC Collaboration**, A. Abada et al., *FCC-hh: The Hadron Collider: Future Circular Collider Conceptual Design Report Volume 3*, Eur. Phys. J. ST **228** (2019), no. 4 755–1107.
- [13] J. Tang et al., *Concept for a Future Super Proton-Proton Collider*, [1507.03224](#).
- [14] W. Konetschny and W. Kummer, *Nonconservation of Total Lepton Number with Scalar Bosons*, Phys. Lett. B **70** (1977) 433–435.
- [15] M. Magg and C. Wetterich, *Neutrino Mass Problem and Gauge Hierarchy*, Phys. Lett. B **94** (1980) 61–64.
- [16] J. Schechter and J. W. F. Valle, *Neutrino Masses in $SU(2) \times U(1)$ Theories*, Phys. Rev. D **22** (1980) 2227.
- [17] T. P. Cheng and L.-F. Li, *Neutrino Masses, Mixings and Oscillations in $SU(2) \times U(1)$ Models of Electroweak Interactions*, Phys. Rev. D **22** (1980) 2860.
- [18] R. N. Mohapatra and G. Senjanovic, *Neutrino Masses and Mixings in Gauge Models with Spontaneous Parity Violation*, Phys. Rev. D **23** (1981) 165.
- [19] G. Lazarides, Q. Shafi, and C. Wetterich, *Proton Lifetime and Fermion Masses in an $SO(10)$ Model*, Nucl. Phys. B **181** (1981) 287–300.
- [20] M. Pospelov, A. Ritz, and M. B. Voloshin, *Secluded WIMP Dark Matter*, Phys. Lett. B **662** (2008) 53–61, [[0711.4866](#)].
- [21] K. J. Kelly and Y. Zhang, *Mononeutrino at DUNE: New Signals from Neutrinophilic Thermal Dark Matter*, Phys. Rev. D **99** (2019), no. 5 055034, [[1901.01259](#)].
- [22] Y. Du, F. Huang, H.-L. Li, and J.-H. Yu, *Freeze-in Dark Matter from Secret Neutrino Interactions*, JHEP **12** (2020) 207, [[2005.01717](#)].

- [23] B. P. Roe, H.-J. Yang, J. Zhu, Y. Liu, I. Stancu, and G. McGregor, *Boosted decision trees, an alternative to artificial neural networks*, Nucl. Instrum. Meth. A **543** (2005), no. 2-3 577–584, [[physics/0408124](#)].
- [24] **Planck Collaboration**, N. Aghanim et al., *Planck 2018 results. VI. Cosmological parameters*, Astron. Astrophys. **641** (2020) A6, [[1807.06209](#)].
- [25] **KATRIN Collaboration**, M. Aker et al., *Improved Upper Limit on the Neutrino Mass from a Direct Kinematic Method by KATRIN*, Phys. Rev. Lett. **123** (2019), no. 22 221802, [[1909.06048](#)].
- [26] **ATLAS Collaboration**, G. Aad et al., *Observation of a new particle in the search for the Standard Model Higgs boson with the ATLAS detector at the LHC*, Phys. Lett. B **716** (2012) 1–29, [[1207.7214](#)].
- [27] **CMS Collaboration**, S. Chatrchyan et al., *Observation of a New Boson at a Mass of 125 GeV with the CMS Experiment at the LHC*, Phys. Lett. B **716** (2012) 30–61, [[1207.7235](#)].
- [28] S. Chakrabarti, D. Choudhury, R. M. Godbole, and B. Mukhopadhyaya, *Observing doubly charged Higgs bosons in photon-photon collisions*, Phys. Lett. B **434** (1998) 347–353, [[hep-ph/9804297](#)].
- [29] E. J. Chun, K. Y. Lee, and S. C. Park, *Testing Higgs triplet model and neutrino mass patterns*, Phys. Lett. B **566** (2003) 142–151, [[hep-ph/0304069](#)].
- [30] A. G. Akeroyd and M. Aoki, *Single and pair production of doubly charged Higgs bosons at hadron colliders*, Phys. Rev. D **72** (2005) 035011, [[hep-ph/0506176](#)].
- [31] P. Fileviez Perez, T. Han, G.-y. Huang, T. Li, and K. Wang, *Neutrino Masses and the CERN LHC: Testing Type II Seesaw*, Phys. Rev. D **78** (2008) 015018, [[0805.3536](#)].
- [32] F. del Aguila and J. A. Aguilar-Saavedra, *Distinguishing seesaw models at LHC with multi-lepton signals*, Nucl. Phys. B **813** (2009) 22–90, [[0808.2468](#)].
- [33] A. G. Akeroyd and H. Sugiyama, *Production of doubly charged scalars from the decay of singly charged scalars in the Higgs Triplet Model*, Phys. Rev. D **84** (2011) 035010, [[1105.2209](#)].
- [34] A. Melfo, M. Nemevsek, F. Nesti, G. Senjanovic, and Y. Zhang, *Type II Seesaw at LHC: The Roadmap*, Phys. Rev. D **85** (2012) 055018, [[1108.4416](#)].
- [35] M. Aoki, S. Kanemura, and K. Yagyu, *Testing the Higgs triplet model with the mass difference at the LHC*, Phys. Rev. D **85** (2012) 055007, [[1110.4625](#)].
- [36] C.-W. Chiang, T. Nomura, and K. Tsumura, *Search for doubly charged Higgs bosons using the same-sign diboson mode at the LHC*, Phys. Rev. D **85** (2012) 095023, [[1202.2014](#)].
- [37] Z.-L. Han, R. Ding, and Y. Liao, *LHC Phenomenology of Type II Seesaw: Nondegenerate Case*, Phys. Rev. D **91** (2015) 093006, [[1502.05242](#)].
- [38] K. S. Babu and S. Jana, *Probing Doubly Charged Higgs Bosons at the LHC through Photon Initiated Processes*, Phys. Rev. D **95** (2017), no. 5 055020, [[1612.09224](#)].
- [39] P. S. B. Dev and Y. Zhang, *Displaced vertex signatures of doubly charged scalars in the type-II seesaw and its left-right extensions*, JHEP **10** (2018) 199, [[1808.00943](#)].
- [40] Y. Du, A. Dunbrack, M. J. Ramsey-Musolf, and J.-H. Yu, *Type-II Seesaw Scalar Triplet Model at a 100 TeV pp Collider: Discovery and Higgs Portal Coupling Determination*, JHEP **01** (2019) 101, [[1810.09450](#)].

- [41] S. Antusch, O. Fischer, A. Hammad, and C. Scherb, *Low scale type II seesaw: Present constraints and prospects for displaced vertex searches*, JHEP **02** (2019) 157, [[1811.03476](#)].
- [42] R. Primulando, J. Julio, and P. Uttayarat, *Scalar phenomenology in type-II seesaw model*, JHEP **08** (2019) 024, [[1903.02493](#)].
- [43] T. B. de Melo, F. S. Queiroz, and Y. Villamizar, *Doubly Charged Scalar at the High-Luminosity and High-Energy LHC*, Int. J. Mod. Phys. A **34** (2019), no. 27 1950157, [[1909.07429](#)].
- [44] R. Padhan, D. Das, M. Mitra, and A. Kumar Nayak, *Probing doubly and singly charged Higgs bosons at the pp collider HE-LHC*, Phys. Rev. D **101** (2020), no. 7 075050, [[1909.10495](#)].
- [45] S. Ashanujjaman and K. Ghosh, *Revisiting Type-II see-saw: Present Limits and Future Prospects at LHC*, [2108.10952](#).
- [46] M. E. Peskin and T. Takeuchi, *A New constraint on a strongly interacting Higgs sector*, Phys. Rev. Lett. **65** (1990) 964–967.
- [47] M. E. Peskin and T. Takeuchi, *Estimation of oblique electroweak corrections*, Phys. Rev. D **46** (1992) 381–409.
- [48] S. Kanemura and K. Yagyu, *Radiative corrections to electroweak parameters in the Higgs triplet model and implication with the recent Higgs boson searches*, Phys. Rev. D **85** (2012) 115009, [[1201.6287](#)].
- [49] E. J. Chun, H. M. Lee, and P. Sharma, *Vacuum Stability, Perturbativity, EWPD and Higgs-to-diphoton rate in Type II Seesaw Models*, JHEP **11** (2012) 106, [[1209.1303](#)].
- [50] **ATLAS Collaboration**, M. Aaboud et al., *Search for doubly charged Higgs boson production in multi-lepton final states with the ATLAS detector using proton–proton collisions at $\sqrt{s} = 13$ TeV*, Eur. Phys. J. C **78** (2018), no. 3 199, [[1710.09748](#)].
- [51] **CMS Collaboration**, *A search for doubly-charged Higgs boson production in three and four lepton final states at $\sqrt{s} = 13$ TeV*, .
- [52] **ATLAS Collaboration**, M. Aaboud et al., *Search for doubly charged scalar bosons decaying into same-sign W boson pairs with the ATLAS detector*, Eur. Phys. J. C **79** (2019), no. 1 58, [[1808.01899](#)].
- [53] **ATLAS Collaboration**, G. Aad et al., *Search for doubly and singly charged Higgs bosons decaying into vector bosons in multi-lepton final states with the ATLAS detector using proton-proton collisions at $\sqrt{s} = 13$ TeV*, [2101.11961](#).
- [54] **HFLAV Collaboration**, Y. Amhis et al., *Averages of b-hadron, c-hadron, and τ -lepton properties as of summer 2016*, Eur. Phys. J. C **77** (2017), no. 12 895, [[1612.07233](#)].
- [55] D. Hanneke, S. Fogwell, and G. Gabrielse, *New Measurement of the Electron Magnetic Moment and the Fine Structure Constant*, Phys. Rev. Lett. **100** (2008) 120801, [[0801.1134](#)].
- [56] **Muon g-2 Collaboration**, G. W. Bennett et al., *Final Report of the Muon E821 Anomalous Magnetic Moment Measurement at BNL*, Phys. Rev. D **73** (2006) 072003, [[hep-ex/0602035](#)].
- [57] **Muon g-2 Collaboration**, B. Abi et al., *Measurement of the Positive Muon Anomalous Magnetic Moment to 0.46 ppm*, Phys. Rev. Lett. **126** (2021), no. 14 141801, [[2104.03281](#)].

- [58] L. Willmann *et al.*, *New bounds from searching for muonium to anti-muonium conversion*, Phys. Rev. Lett. **82** (1999) 49–52, [[hep-ex/9807011](#)].
- [59] **DELPHI Collaboration**, J. Abdallah *et al.*, *Measurement and interpretation of fermion-pair production at LEP energies above the Z resonance*, Eur. Phys. J. C **45** (2006) 589–632, [[hep-ex/0512012](#)].
- [60] M. Lindner, M. Platscher, and F. S. Queiroz, *A Call for New Physics : The Muon Anomalous Magnetic Moment and Lepton Flavor Violation*, Phys. Rept. **731** (2018) 1–82, [[1610.06587](#)].
- [61] T. Aoyama *et al.*, *The anomalous magnetic moment of the muon in the Standard Model*, Phys. Rept. **887** (2020) 1–166, [[2006.04822](#)].
- [62] P. S. B. Dev, R. N. Mohapatra, and Y. Zhang, *Lepton Flavor Violation Induced by a Neutral Scalar at Future Lepton Colliders*, Phys. Rev. Lett. **120** (2018), no. 22 221804, [[1711.08430](#)].
- [63] P. S. Bhupal Dev, R. N. Mohapatra, and Y. Zhang, *Probing TeV scale origin of neutrino mass at future lepton colliders via neutral and doubly-charged scalars*, Phys. Rev. D **98** (2018), no. 7 075028, [[1803.11167](#)].
- [64] T. Li and M. A. Schmidt, *Sensitivity of future lepton colliders to the search for charged lepton flavor violation*, Phys. Rev. D **99** (2019), no. 5 055038, [[1809.07924](#)].
- [65] J. A. Evans, P. Tanedo, and M. Zakeri, *Exotic Lepton-Flavor Violating Higgs Decays*, JHEP **01** (2020) 028, [[1910.07533](#)].
- [66] S. Iguro, Y. Omura, and M. Takeuchi, *Probing $\mu\tau$ flavor-violating solutions for the muon $g - 2$ anomaly at Belle II*, JHEP **09** (2020) 144, [[2002.12728](#)].
- [67] T. Li, M. A. Schmidt, C.-Y. Yao, and M. Yuan, *Charged lepton flavor violation in light of the muon magnetic moment anomaly and colliders*, [[2104.04494](#)].
- [68] W.-S. Hou and G. Kumar, *Charged lepton flavor violation in light of Muon $g - 2$* , [[2107.14114](#)].
- [69] R. Capdevilla, D. Curtin, Y. Kahn, and G. Krnjaic, *Discovering the physics of $(g - 2)_\mu$ at future muon colliders*, Phys. Rev. D **103** (2021), no. 7 075028, [[2006.16277](#)].
- [70] D. Buttazzo and P. Paradisi, *Probing the muon $g-2$ anomaly at a Muon Collider*, [[2012.02769](#)].
- [71] W. Yin and M. Yamaguchi, *Muon $g - 2$ at multi-TeV muon collider*, [[2012.03928](#)].
- [72] R. Capdevilla, D. Curtin, Y. Kahn, and G. Krnjaic, *A No-Lose Theorem for Discovering the New Physics of $(g - 2)_\mu$ at Muon Colliders*, [[2101.10334](#)].
- [73] G. Haghight and M. Mohammadi Najafabadi, *Search for lepton-flavor-violating ALPs at a future muon collider and utilization of polarization-induced effects*, [[2106.00505](#)].
- [74] H. Fusaoka and Y. Koide, *Updated estimate of running quark masses*, Phys. Rev. D **57** (1998) 3986–4001, [[hep-ph/9712201](#)].
- [75] Z.-z. Xing, H. Zhang, and S. Zhou, *Updated Values of Running Quark and Lepton Masses*, Phys. Rev. D **77** (2008) 113016, [[0712.1419](#)].
- [76] Z.-z. Xing, H. Zhang, and S. Zhou, *Impacts of the Higgs mass on vacuum stability, running fermion masses and two-body Higgs decays*, Phys. Rev. D **86** (2012) 013013, [[1112.3112](#)].

- [77] S. Antusch and V. Maurer, *Running quark and lepton parameters at various scales*, JHEP **11** (2013) 115, [[1306.6879](#)].
- [78] G.-y. Huang and S. Zhou, *Precise Values of Running Quark and Lepton Masses in the Standard Model*, Phys. Rev. D **103** (2021), no. 1 016010, [[2009.04851](#)].
- [79] N. Arkani-Hamed, T. Han, M. Mangano, and L.-T. Wang, *Physics opportunities of a 100 TeV proton–proton collider*, Phys. Rept. **652** (2016) 1–49, [[1511.06495](#)].
- [80] A. Alloul, N. D. Christensen, C. Degrande, C. Duhr, and B. Fuks, *FeynRules 2.0 - A complete toolbox for tree-level phenomenology*, Comput. Phys. Commun. **185** (2014) 2250–2300, [[1310.1921](#)].
- [81] J. Alwall, R. Frederix, S. Frixione, V. Hirschi, F. Maltoni, O. Mattelaer, H. S. Shao, T. Stelzer, P. Torrielli, and M. Zaro, *The automated computation of tree-level and next-to-leading order differential cross sections, and their matching to parton shower simulations*, JHEP **07** (2014) 079, [[1405.0301](#)].
- [82] P. Artoisenet, R. Frederix, O. Mattelaer, and R. Rietkerk, *Automatic spin-entangled decays of heavy resonances in Monte Carlo simulations*, JHEP **03** (2013) 015, [[1212.3460](#)].
- [83] M. Muhlleitner and M. Spira, *A Note on doubly charged Higgs pair production at hadron colliders*, Phys. Rev. D **68** (2003) 117701, [[hep-ph/0305288](#)].
- [84] T. Sjostrand, S. Mrenna, and P. Z. Skands, *A Brief Introduction to PYTHIA 8.1*, Comput. Phys. Commun. **178** (2008) 852–867, [[0710.3820](#)].
- [85] M. Cacciari, G. P. Salam, and G. Soyez, *FastJet User Manual*, Eur. Phys. J. C **72** (2012) 1896, [[1111.6097](#)].
- [86] M. Cacciari, G. P. Salam, and G. Soyez, *The anti- k_t jet clustering algorithm*, JHEP **04** (2008) 063, [[0802.1189](#)].
- [87] **DELPHES 3 Collaboration**, J. de Favereau, C. Delaere, P. Demin, A. Giammanco, V. Lemaître, A. Mertens, and M. Selvaggi, *DELPHES 3, A modular framework for fast simulation of a generic collider experiment*, JHEP **02** (2014) 057, [[1307.6346](#)].
- [88] V. D. Barger, T. Han, and J. Ohnemus, *HEAVY LEPTONS AT HADRON SUPERCOLLIDERS*, Phys. Rev. D **37** (1988) 1174.
- [89] **ATLAS Collaboration**, *Search for squarks and gluinos in final states with an isolated lepton, jets, and missing transverse momentum at $\sqrt{s} = 13$ TeV with the ATLAS detector*, .
- [90] **ATLAS Collaboration**, *Search for new phenomena in final states with large jet multiplicities and missing transverse momentum using $\sqrt{s} = 13$ TeV proton-proton collisions recorded by ATLAS in Run 2 of the LHC*, .
- [91] T. Chen and C. Guestrin, *XGBoost: A Scalable Tree Boosting System*, [1603.02754](#).
- [92] **OPAL Collaboration**, G. Abbiendi et al., *Search for doubly charged Higgs bosons with the OPAL detector at LEP*, Phys. Lett. B **526** (2002) 221–232, [[hep-ex/0111059](#)].
- [93] **DELPHI Collaboration**, J. Abdallah et al., *Search for doubly charged Higgs bosons at LEP-2*, Phys. Lett. B **552** (2003) 127–137, [[hep-ex/0303026](#)].
- [94] **L3 Collaboration**, P. Achard et al., *Search for doubly charged Higgs bosons at LEP*, Phys. Lett. B **576** (2003) 18–28, [[hep-ex/0309076](#)].

- [95] **CDF Collaboration**, D. Acosta *et al.*, *Search for doubly-charged Higgs bosons decaying to dileptons in $p\bar{p}$ collisions at $\sqrt{s} = 1.96$ TeV*, Phys. Rev. Lett. **93** (2004) 221802, [[hep-ex/0406073](#)].
- [96] **CDF Collaboration**, T. Aaltonen *et al.*, *Search for Doubly Charged Higgs Bosons with Lepton-Flavor-Violating Decays involving Tau Leptons*, Phys. Rev. Lett. **101** (2008) 121801, [[0808.2161](#)].
- [97] **D0 Collaboration**, V. M. Abazov *et al.*, *Search for pair production of doubly-charged Higgs bosons in the $H^{++}H^{--} \rightarrow \mu^+\mu^+\mu^-\mu^-$ final state at D0*, Phys. Rev. Lett. **101** (2008) 071803, [[0803.1534](#)].
- [98] **D0 Collaboration**, V. M. Abazov *et al.*, *Search for doubly-charged Higgs boson pair production in $p\bar{p}$ collisions at $\sqrt{s} = 1.96$ TeV*, Phys. Rev. Lett. **108** (2012) 021801, [[1106.4250](#)].
- [99] **ATLAS Collaboration**, *Search for Doubly Charged Higgs Boson Production in Like-sign Muon Pairs in pp Collisions at $\sqrt{s}=7$ TeV*, .
- [100] **CMS Collaboration**, *Inclusive search for doubly charged higgs in leptonic final states at $\sqrt{s}=7$ TeV*, .
- [101] **ATLAS Collaboration**, G. Aad *et al.*, *Search for anomalous production of prompt same-sign lepton pairs and pair-produced doubly charged Higgs bosons with $\sqrt{s} = 8$ TeV pp collisions using the ATLAS detector*, JHEP **03** (2015) 041, [[1412.0237](#)].
- [102] **CMS Collaboration**, *Search for a doubly-charged Higgs boson with $\sqrt{s} = 8$ TeV pp collisions at the CMS experiment*, .
- [103] B. Gripaios, *Transverse observables and mass determination at hadron colliders*, JHEP **02** (2008) 053, [[0709.2740](#)].
- [104] A. J. Barr, B. Gripaios, and C. G. Lester, *Weighing Wimps with Kinks at Colliders: Invisible Particle Mass Measurements from Endpoints*, JHEP **02** (2008) 014, [[0711.4008](#)].
- [105] D. Curtin, *Mixing It Up With MT2: Unbiased Mass Measurements at Hadron Colliders*, Phys. Rev. D **85** (2012) 075004, [[1112.1095](#)].
- [106] F. Lyonnet, I. Schienbein, F. Staub, and A. Wingerter, *PyR@TE: Renormalization Group Equations for General Gauge Theories*, Comput. Phys. Commun. **185** (2014) 1130–1152, [[1309.7030](#)].
- [107] H. Arason, D. J. Castano, B. Keszthelyi, S. Mikaelian, E. J. Piard, P. Ramond, and B. D. Wright, *Renormalization group study of the standard model and its extensions. 1. The Standard model*, Phys. Rev. D **46** (1992) 3945–3965.
- [108] A. Arhrib, R. Benbrik, M. Chabab, G. Moulhaka, M. C. Peyranere, L. Rahili, and J. Ramadan, *The Higgs Potential in the Type II Seesaw Model*, Phys. Rev. **D84** (2011) 095005, [[1105.1925](#)].